

Fracture analysis of cracks in magneto-electro-elastic solids by the MLPG

J. Sladek · V. Sladek · P. Sulek · E. Pan

Received: 12 December 2007 / Accepted: 3 March 2008 / Published online: 26 March 2008
© Springer-Verlag 2008

Abstract A meshless method based on the local Petrov–Galerkin approach is proposed for crack analysis in two-dimensional (2-D) and three-dimensional (3-D) axisymmetric magneto-electric-elastic solids with continuously varying material properties. Axial symmetry of geometry and boundary conditions reduces the original 3-D boundary value problem into a 2-D problem in axial cross section. Stationary and transient dynamic problems are considered in this paper. The local weak formulation is employed on circular subdomains where surrounding nodes randomly spread over the analyzed domain. The test functions are taken as unit step functions in derivation of the local integral equations (LIEs). The moving least-squares (MLS) method is adopted for the approximation of the physical quantities in the LIEs. The accuracy of the present method for computing the stress intensity factors (SIF), electrical displacement intensity factors (EDIF) and magnetic induction intensity factors (MIIF) are discussed by comparison with numerical solutions for homogeneous materials.

Keywords Magneto-electric-elastic solids · Meshless local Petrov–Galerkin method (MLPG) · Moving least-squares (MLS) interpolation · Cracks · Intensity factors ·

2-D and 3-D axisymmetric dynamic problems · Permeable and impermeable conditions

1 Introduction

Modern smart structures made of piezoelectric and piezomagnetic materials offer certain potential performance advantages over conventional ones due to their capability of converting the energy from one type to other (among magnetic, electric, and mechanical) [5, 7, 21, 26]. Former activities were focused on modeling of magneto-electric-elastic fields to determine the field variables [1, 9, 24, 29, 43]. Recently, increasing interest is devoted to fracture mechanics of magneto-electric-elastic materials [16, 20, 36, 40, 41, 45, 46, 48]. All above mentioned works are made under a static deformation assumption. However, dynamic fracture analyses are occurring in literature very seldom. Some works on relatively simple anti-plane problems have been published [11, 13, 38]. Three-dimensional (3-D) penny-shaped crack problem under a static load has been analyzed by Zhao et al. [47]. Recently, Feng et al. [14] have investigated the transient response of a penny-shaped crack embedded in a magneto-electro-thermo-elastic layer of a finite thickness. Coupling of magneto-electro-thermo-elastic fields is investigated in works [27, 49].

While the piezoelectric and piezomagnetic effects are due to electro-elastic and magneto-elastic interaction, respectively, the magnetoelectric effect is the induction of the electrical polarization by magnetic field and the induction of magnetization by electric field via electro-magneto-elastic interactions. Magnetoelectric coupling plays an important role in the dynamic behavior of certain materials, especially compounds which possess simultaneously ferroelectric and ferromagnetic phases [12]. The electric and magnetic

J. Sladek (✉) · V. Sladek
Institute of Construction and Architecture,
Slovak Academy of Sciences,
84503 Bratislava, Slovakia
e-mail: sladek@savba.sk

P. Sulek
Department of Mechanics,
Slovak Technical University, Bratislava, Slovakia

E. Pan
Computer Modeling and Simulation Group,
Department of Civil Engineering, University of Akron,
Akron, OH 44325-3905, USA

symmetry groups for certain crystals permit the piezoelectric and piezomagnetic as well as magnetoelectric effects. In centrosymmetric crystals neither of these effects exists. However, remarkably large magnetoelectric effects are observed in composites rather than in either single phase/constituent [13,26]. If the volume fraction of constituents is varying in a predominant direction we are talking about functionally graded materials (FGMs). Originally these materials have been introduced to benefit from the ideal performance of its constituents, e.g., high heat and corrosion resistance of ceramics on one side, and large mechanical strength and toughness of metals on the other side. A review on various aspects of FGMs can be found in the monograph of Suresh and Mortensen [39] and the review chapter by Paulino et al. [31]. Later, the demand for piezoelectric materials with high strength, high toughness, low thermal expansion coefficient and low dielectric constant encourages the study of functionally graded piezoelectric materials [19,42,50]. According to the best of authors' knowledge there is available only one paper [13] with applications to continuously nonhomogeneous magneto-electric materials. The dynamic anti-plane crack problem with exponential variation of material properties is analyzed by Feng and Su [13] analytically for a cracked infinite strip.

The solution of general boundary value problems for continuously nonhomogeneous magneto-electric-elastic solids requires advanced numerical methods due to the high mathematical complexity. Besides this complication, the magnetic, electric and mechanical fields are coupled with each other in the constitutive equations. In spite of the great success of the finite element method (FEM) and boundary element method (BEM) as effective numerical tools for the solution of boundary value problems in magneto-electric-elastic solids, there is still a growing interest in the development of new advanced numerical methods. In recent years, meshless formulations are becoming popular due to their high adaptability and low costs to prepare input and output data in numerical analysis. The moving least squares (MLS) approximation is generally considered as one of many schemes to interpolate discrete data with a reasonable accuracy. The continuity of the MLS approximation is given by the minimum between the continuity of the basis functions and that of the weight function. So continuity can be tuned to a desired value. In conventional discretization methods there is a discontinuity of secondary fields (gradients of primary fields) on the interface of elements. For modeling of continuously nonhomogeneous solids the approach based on piecewise continuous elements can bring some inaccuracies. Therefore, modeling based on C^1 continuity, like meshless methods, is expected to be more accurate than conventional discretization techniques. The meshless or generalized FEM methods are also very convenient for modeling of cracks. One can embed particular enrichment functions at the crack tip so the

stress intensity factor can be accurately predicted [15]. Meshless methods can easily simulate crack propagation without remeshing [22].

A variety of meshless methods has been proposed so far with some of them applied only to piezoelectric problems [25,28]. They can be derived either from a weak-form formulation on the global domain or on a set of local subdomains. In the global formulation, background cells are required for the integration of the weak-form. In methods based on local weak-form formulation, no background cells are required and therefore they are often referred to as truly meshless methods. The meshless local Petrov–Galerkin (MLPG) method is a fundamental base for the derivation of many meshless formulations, since trial and test functions can be chosen from different functional spaces. Recently, the MLPG method with a Heaviside step function as the test functions [2–4,32] has been applied to solve two-dimensional (2-D) homogeneous piezoelectric problems [33]. In the present paper, the MLPG method is extended to 2-D and 3-D axisymmetric and continuously nonhomogeneous magneto-electric-elastic solids with cracks. The coupled governing partial differential equations are satisfied in a weak form on small fictitious subdomains. Nodal points are introduced and spread on the analyzed domain and each node is surrounded by a small circle for simplicity, but without loss of generality. For a simple shape of subdomains like circles applied in this paper, numerical integrations over them can be easily carried out. The integral equations have a very simple nonsingular form. The spatial variations of the displacements, the electric and magnetic potentials are approximated by the (MLS) scheme [2,6]. After performing the spatial integrations, a system of linear algebraic equations for the unknown nodal values is obtained. The essential boundary conditions on the global boundary are satisfied by the collocation of the MLS-approximation expressions for the displacements, electric and magnetic potentials at the boundary nodal points. The accuracy and the efficiency of the proposed MLPG method are verified by several numerical examples for computing the stress intensity factors (SIF), electrical displacement intensity factor (EDIF) and magnetic induction intensity factor (MIIF). Numerical results are presented and compared with available FEM numerical solutions for homogeneous materials.

2 Local boundary integral equations for 2-D problems

2.1 Physical and mathematical model

Basic equations of phenomenological theory of nonconducting elastic materials consist of the governing equations (Maxwell's equations, the balance of momentum) and the constitutive relationships. The governing equations comple-

ted by the boundary and initial conditions should be solved for unknown primary field variables such as the elastic displacement vector field $u_i(\mathbf{x}, \tau)$, the electric potential $\psi(\mathbf{x}, \tau)$ (or its gradient called the electric vector field $E_i(\mathbf{x}, \tau)$), and the magnetic potential $\mu(\mathbf{x}, \tau)$ (or its gradient called the magnetic intensity field $H_i(\mathbf{x}, \tau)$). The constitutive equations co-relate the primary fields $\{u_i, E_i, H_i\}$ with the secondary fields $\{\sigma_{ij}, D_i, B_i\}$ which are the stress tensor field, the electric displacement vector field, and the magnetic induction vector field, respectively. The governing equations give not only the relationships between conjugated fields in each of the pairs $(\sigma_{ij}, \varepsilon_{ij})$, (D_i, E_i) , (B_i, H_i) , but describe also the electro-magneto-elastic interactions in the phenomenological theory of continuous solids.

Taking into account the typical material coefficients, it can be found that characteristic frequencies for elastic and electromagnetic processes are $f_{el} = 10^4$ Hz and $f_{elm} = 10^7$ Hz, respectively. Thus, if we consider such bodies under transient loadings with temporal changes corresponding to f_{el} , the changes of the electromagnetic fields can be assumed to be immediate, or in other words the electromagnetic fields can be considered like quasi-static [30]. Then, the Maxwell equations are reduced to two scalar equations

$$D_{j,j}(\mathbf{x}, \tau) = 0, \quad (1)$$

$$B_{j,j}(\mathbf{x}, \tau) = 0. \quad (2)$$

The rest vector Maxwell's equations in quasi-static approximation, $\nabla \times \mathbf{E} = 0$ and $\nabla \times \mathbf{H} = 0$, are satisfied identically by appropriate representation of the fields $\mathbf{E}(\mathbf{x}, \tau)$ and $\mathbf{H}(\mathbf{x}, \tau)$ as gradients of scalar electric and magnetic potentials $\psi(\mathbf{x}, \tau)$ and $\mu(\mathbf{x}, \tau)$, respectively,

$$E_j(\mathbf{x}, \tau) = -\psi_{,j}(\mathbf{x}, \tau), \quad (3)$$

$$H_j(\mathbf{x}, \tau) = -\mu_{,j}(\mathbf{x}, \tau). \quad (4)$$

To complete the set of governing equations, Eqs. (1) and (2) need to be supplied by the equation of motion in elastic continuum

$$\sigma_{ij,j}(\mathbf{x}, \tau) + X_i(\mathbf{x}, \tau) = \rho \ddot{u}_i(\mathbf{x}, \tau), \quad (5)$$

where \ddot{u}_i , ρ and X_i denote the acceleration of displacements, the mass density, and the body force vector, respectively. A comma after a quantity represents the partial derivatives of the quantity and a dot is used for the time derivative.

Finally, we extend the constitutive equations involving the general electro-magneto-elastic interaction [26] to media with spatially dependent material coefficients for continuously nonhomogeneous media

$$\sigma_{ij}(\mathbf{x}, \tau) = c_{ijkl}(\mathbf{x})\varepsilon_{kl}(\mathbf{x}, \tau) - e_{kij}(\mathbf{x})E_k(\mathbf{x}, \tau) - d_{kij}(\mathbf{x})H_k(\mathbf{x}, \tau), \quad (6)$$

$$D_j(\mathbf{x}, \tau) = e_{jkl}(\mathbf{x})\varepsilon_{kl}(\mathbf{x}, \tau) + h_{jk}(\mathbf{x})E_k(\mathbf{x}, \tau) + \alpha_{jk}(\mathbf{x})H_k(\mathbf{x}, \tau), \quad (7)$$

$$B_j(\mathbf{x}, \tau) = d_{jkl}(\mathbf{x})\varepsilon_{kl}(\mathbf{x}, \tau) + \alpha_{kj}(\mathbf{x})E_k(\mathbf{x}, \tau) + \gamma_{jk}(\mathbf{x})H_k(\mathbf{x}, \tau), \quad (8)$$

with the strain tensor ε_{ij} being related to the displacements u_i by

$$\varepsilon_{ij} = \frac{1}{2}(u_{i,j} + u_{j,i}). \quad (9)$$

The functional coefficients $c_{ijkl}(\mathbf{x})$, $h_{jk}(\mathbf{x})$, and $\gamma_{jk}(\mathbf{x})$ are the elastic coefficients, dielectric permittivities, and magnetic permeabilities, respectively; $e_{kij}(\mathbf{x})$, $d_{kij}(\mathbf{x})$, and $\alpha_{jk}(\mathbf{x})$ are the piezoelectric, piezomagnetic, and magnetoelectric coefficients, respectively. Owing to transient loadings, inertial effects and coupling, the elastic fields as well as electro-magnetic fields are time dependent, though the fields E_i and H_i are treated in quasi-static approximation.

In case of some crystal symmetries, one can formulate also the plane-deformation problems [30]. For instance, in the crystals of hexagonal symmetry (class 6mm) with x_3 being the 6-order symmetry axis and assuming $u_2 = 0$ as well as the independence on x_2 , i.e., $(\cdot)_{,2} = 0$, we have $\varepsilon_{22} = \varepsilon_{23} = \varepsilon_{12} = E_2 = H_2 = 0$. Then, the constitutive equations (6)–(8) are reduced to the following form

$$\begin{aligned} \begin{bmatrix} \sigma_{11} \\ \sigma_{33} \\ \sigma_{13} \end{bmatrix} &= \begin{bmatrix} c_{11} & c_{13} & 0 \\ c_{13} & c_{33} & 0 \\ 0 & 0 & c_{44} \end{bmatrix} \begin{bmatrix} \varepsilon_{11} \\ \varepsilon_{33} \\ 2\varepsilon_{13} \end{bmatrix} - \begin{bmatrix} 0 & e_{31} \\ 0 & e_{33} \\ e_{15} & 0 \end{bmatrix} \begin{bmatrix} E_1 \\ E_3 \end{bmatrix} \\ &\quad - \begin{bmatrix} 0 & d_{31} \\ 0 & d_{33} \\ d_{15} & 0 \end{bmatrix} \begin{bmatrix} H_1 \\ H_3 \end{bmatrix} \\ &= \mathbf{C}(\mathbf{x}) \begin{bmatrix} \varepsilon_{11} \\ \varepsilon_{33} \\ 2\varepsilon_{13} \end{bmatrix} - \mathbf{L}(\mathbf{x}) \begin{bmatrix} E_1 \\ E_3 \end{bmatrix} - \mathbf{K}(\mathbf{x}) \begin{bmatrix} H_1 \\ H_3 \end{bmatrix}, \end{aligned} \quad (10)$$

$$\begin{aligned} \begin{bmatrix} D_1 \\ D_3 \end{bmatrix} &= \begin{bmatrix} 0 & 0 & e_{15} \\ e_{31} & e_{33} & 0 \end{bmatrix} \begin{bmatrix} \varepsilon_{11} \\ \varepsilon_{33} \\ 2\varepsilon_{13} \end{bmatrix} + \begin{bmatrix} h_{11} & 0 \\ 0 & h_{33} \end{bmatrix} \begin{bmatrix} E_1 \\ E_3 \end{bmatrix} \\ &\quad + \begin{bmatrix} \alpha_{11} & 0 \\ 0 & \alpha_{33} \end{bmatrix} \begin{bmatrix} H_1 \\ H_3 \end{bmatrix} \\ &= \mathbf{G}(\mathbf{x}) \begin{bmatrix} \varepsilon_{11} \\ \varepsilon_{33} \\ 2\varepsilon_{13} \end{bmatrix} + \mathbf{H}(\mathbf{x}) \begin{bmatrix} E_1 \\ E_3 \end{bmatrix} + \mathbf{A}(\mathbf{x}) \begin{bmatrix} H_1 \\ H_3 \end{bmatrix}, \end{aligned} \quad (11)$$

$$\begin{aligned} \begin{bmatrix} B_1 \\ B_3 \end{bmatrix} &= \begin{bmatrix} 0 & 0 & d_{15} \\ d_{31} & d_{33} & 0 \end{bmatrix} \begin{bmatrix} \varepsilon_{11} \\ \varepsilon_{33} \\ 2\varepsilon_{13} \end{bmatrix} + \begin{bmatrix} \alpha_{11} & 0 \\ 0 & \alpha_{33} \end{bmatrix} \begin{bmatrix} E_1 \\ E_3 \end{bmatrix} \\ &\quad + \begin{bmatrix} \gamma_{11} & 0 \\ 0 & \gamma_{33} \end{bmatrix} \begin{bmatrix} H_1 \\ H_3 \end{bmatrix} \\ &= \mathbf{R}(\mathbf{x}) \begin{bmatrix} \varepsilon_{11} \\ \varepsilon_{33} \\ 2\varepsilon_{13} \end{bmatrix} + \mathbf{A}(\mathbf{x}) \begin{bmatrix} E_1 \\ E_3 \end{bmatrix} + \mathbf{M}(\mathbf{x}) \begin{bmatrix} H_1 \\ H_3 \end{bmatrix}. \end{aligned} \quad (12)$$

Recall that σ_{22} does not influence the governing equations, although it is not vanishing in general, since $\sigma_{22} = c_{12}\varepsilon_{11} + c_{13}\varepsilon_{33} - e_{13}E_3$.

The following essential and natural boundary conditions are assumed for the mechanical field

$$\begin{aligned} u_i(\mathbf{x}, \tau) &= \tilde{u}_i(\mathbf{x}, \tau), \quad \text{on } \Gamma_u, \\ t_i(\mathbf{x}, \tau) &= \sigma_{ij}n_j = \tilde{t}_i(\mathbf{x}, \tau), \quad \text{on } \Gamma_t, \Gamma = \Gamma_u \cup \Gamma_t. \end{aligned}$$

For the electrical field, we assume

$$\begin{aligned} \psi(\mathbf{x}, \tau) &= \tilde{\psi}(\mathbf{x}, \tau), \quad \text{on } \Gamma_p, \\ n_i(\mathbf{x})D_i(\mathbf{x}, \tau) &\equiv Q(\mathbf{x}, \tau) = \tilde{Q}(\mathbf{x}, \tau), \quad \text{on } \Gamma_q, \Gamma = \Gamma_p \cup \Gamma_q \end{aligned}$$

and for the magnetic field

$$\begin{aligned} \mu(\mathbf{x}, \tau) &= \tilde{\mu}(\mathbf{x}, \tau), \quad \text{on } \Gamma_a, \\ n_i(\mathbf{x})B_i(\mathbf{x}, \tau) &\equiv S(\mathbf{x}, \tau) = \tilde{S}(\mathbf{x}, \tau), \quad \text{on } \Gamma_b, \Gamma = \Gamma_a \cup \Gamma_b, \end{aligned}$$

where Γ_u is the part of the global boundary Γ with prescribed displacements, while on $\Gamma_t, \Gamma_p, \Gamma_q, \Gamma_a$, and Γ_b the traction vector, the electric potential, the normal component of the electric displacement vector, the magnetic potential and the magnetic flux are prescribed, respectively. Recall that $\tilde{Q}(\mathbf{x}, \tau)$ can be considered approximately as the surface density of free charge, provided that the permittivity of the solid is much greater than that of the surrounding medium (vacuum).

The initial conditions for the mechanical displacements are assumed as

$$u_i(\mathbf{x}, \tau)|_{\tau=0} = u_i(\mathbf{x}, 0) \quad \text{and} \quad \dot{u}_i(\mathbf{x}, \tau)|_{\tau=0} = \dot{u}_i(\mathbf{x}, 0) \quad \text{in } \Omega.$$

2.2 Formulation for solution of the boundary—initial problems

Applying the Laplace-transform to the governing equations (5) one obtains

$$\bar{\sigma}_{ij,j}(\mathbf{x}, p) - \rho(\mathbf{x})p^2\bar{u}_i(\mathbf{x}, p) = -\bar{F}_i(\mathbf{x}, p), \quad (13)$$

where

$$\bar{F}_i(\mathbf{x}, p) = \bar{X}_i(\mathbf{x}, p) + pu_i(\mathbf{x}, 0) + \dot{u}_i(\mathbf{x}, 0),$$

is the re-defined body force in the Laplace-transformed domain with the initial boundary conditions for the displacements $u_i(\mathbf{x}, 0)$ and velocities $\dot{u}_i(\mathbf{x}, 0)$. Recall that the subscripts take now values $i \in \{1, 3\}$.

The Laplace-transform of a function $f(\mathbf{x}, \tau)$ is defined as

$$L[f(\mathbf{x}, \tau)] = \bar{f}(\mathbf{x}, p) = \int_0^\infty f(\mathbf{x}, \tau)e^{-p\tau}d\tau,$$

where p is the Laplace-transform parameter.

Instead of writing the global weak-form for the above governing equations, the MLPG method constructs a weak-form

over the local fictitious subdomains such as Ω_s , which is a small region constructed for each node inside the global domain [2]. The local subdomains overlap each other, and cover the whole global domain Ω . The local subdomains could be of any geometrical shape and size. In the present paper, the local subdomains are taken to be of a circular shape for simplicity. The local weak-form of the governing equation (13) can be written as

$$\int_{\Omega_s} [\bar{\sigma}_{ij,j}(\mathbf{x}, p) - \rho(\mathbf{x})p^2\bar{u}_i(\mathbf{x}, p) + \bar{F}_i(\mathbf{x}, p)] u_{ik}^*(\mathbf{x}) d\Omega = 0, \quad (14)$$

where $u_{ik}^*(\mathbf{x})$ is a test function.

Using

$$\sigma_{ij,j}u_{ik}^* = (\sigma_{ij}u_{ik}^*)_{,j} - \sigma_{ij}u_{ik,j}^*$$

and applying the Gauss divergence theorem to Eq. (14) one obtains

$$\begin{aligned} \int_{\partial\Omega_s} \bar{\sigma}_{ij}(\mathbf{x}, p)n_j(\mathbf{x})u_{ik}^*(\mathbf{x})d\Gamma - \int_{\Omega_s} \bar{\sigma}_{ij}(\mathbf{x}, p)u_{ik,j}^*(\mathbf{x})d\Omega \\ + \int_{\Omega_s} [\bar{F}_i(\mathbf{x}, p) - \rho(\mathbf{x})p^2\bar{u}_i(\mathbf{x}, p)] u_{ik}^*(\mathbf{x})d\Omega = 0, \quad (15) \end{aligned}$$

where $\partial\Omega_s$ is the boundary of the local subdomain which consists of three parts $\partial\Omega_s = L_s \cup \Gamma_{st} \cup \Gamma_{su}$ [2]. Here, L_s is the local boundary that is totally inside the global domain, Γ_{st} is the part of the local boundary which coincides with the global traction boundary, i.e., $\Gamma_{st} = \partial\Omega_s \cap \Gamma_t$, and similarly Γ_{su} is the part of the local boundary that coincides with the global displacement boundary, i.e., $\Gamma_{su} = \partial\Omega_s \cap \Gamma_u$.

By choosing a Heaviside step function as the test function $u_{ik}^*(\mathbf{x})$ in each subdomain as

$$u_{ik}^*(\mathbf{x}) = \begin{cases} \delta_{ik} & \text{at } \mathbf{x} \in \Omega_s \\ 0 & \text{at } \mathbf{x} \notin \Omega_s \end{cases},$$

the local weak-form (15) is converted into the following local boundary-domain integral equations

$$\begin{aligned} \int_{L_s + \Gamma_{su}} \bar{t}_i(\mathbf{x}, p)d\Gamma - \int_{\Omega_s} \rho(\mathbf{x})p^2\bar{u}_i(\mathbf{x}, p)d\Omega \\ = - \int_{\Gamma_{st}} \bar{\tilde{t}}_i(\mathbf{x}, p)d\Gamma - \int_{\Omega_s} \bar{F}_i(\mathbf{x}, p)d\Omega. \quad (16) \end{aligned}$$

Equation (16) is recognized as the overall force equilibrium conditions on the subdomain Ω_s . Note that the local integral equation (LIE) (16) is valid for both the homogeneous and nonhomogeneous solids. Nonhomogeneous material properties are included in Eq. (16) through the elastic, piezoelectric and piezomagnetic coefficients in the traction components.

Similarly, the local weak-form of the governing equation (2) can be written as

$$\int_{\Omega_s} \bar{D}_{j,j}(\mathbf{x}, p) v^*(\mathbf{x}) d\Omega = 0, \quad (17)$$

where $v^*(\mathbf{x})$ is a test function.

Applying the Gauss divergence theorem to the local weak-form (17) and choosing the Heaviside step function as the test function $v^*(\mathbf{x})$ one can obtain

$$\int_{L_s + \Gamma_{sp}} \bar{Q}(\mathbf{x}, p) d\Gamma = - \int_{\Gamma_{sq}} \bar{Q}(\mathbf{x}, p) d\Gamma, \quad (18)$$

where

$$\begin{aligned} \bar{Q}(\mathbf{x}, p) &= \bar{D}_j(\mathbf{x}, p) n_j(\mathbf{x}) \\ &= [e_{jkl} \bar{u}_{k,l}(\mathbf{x}, p) - h_{jk} \bar{\psi}_{,k}(\mathbf{x}, p) - \alpha_{jk} \bar{\mu}_{,k}(\mathbf{x}, p)] n_j. \end{aligned}$$

The LIE corresponding to the third governing equation (3) has the form

$$\int_{L_s + \Gamma_{sa}} \bar{S}(\mathbf{x}, p) d\Gamma = - \int_{\Gamma_{sb}} \bar{S}(\mathbf{x}, p) d\Gamma, \quad (19)$$

where magnetic flux is given by

$$\begin{aligned} \bar{S}(\mathbf{x}, p) &= \bar{B}_j(\mathbf{x}, p) n_j(\mathbf{x}) \\ &= [d_{jkl} \bar{u}_{k,l}(\mathbf{x}, p) - \alpha_{kj} \bar{\psi}_{,k}(\mathbf{x}, p) - \gamma_{jk} \bar{\mu}_{,k}(\mathbf{x}, p)] n_j. \end{aligned}$$

In the MLPG method the test and the trial functions are not necessarily from the same functional spaces. For internal nodes, the test function is chosen as the Heaviside step function with its support on the local subdomain. The trial functions, on the other hand, are chosen to be the MLS approximations by using a number of nodes spreading over the domain of influence. According to the MLS [6] method, the approximation of the displacement can be given as

$$\mathbf{u}^h(\mathbf{x}) = \sum_{i=1}^m p_i(\mathbf{x}) \mathbf{a}_i(\mathbf{x}) = \mathbf{p}^T(\mathbf{x}) \mathbf{a}(\mathbf{x}),$$

where $\mathbf{p}^T(\mathbf{x}) = \{p_1(\mathbf{x}), p_2(\mathbf{x}), \dots, p_m(\mathbf{x})\}$ is a vector of complete basis functions of order m and $\mathbf{a}(\mathbf{x}) = \{\mathbf{a}_1(\mathbf{x}), \mathbf{a}_2(\mathbf{x}), \dots, \mathbf{a}_m(\mathbf{x})\}$ is a vector of unknown parameters that depend on \mathbf{x} . For example, in 2-D problems

$$\mathbf{p}^T(\mathbf{x}) = \{1, x_1, x_2\} \quad \text{for } m = 3$$

and

$$\mathbf{p}^T(\mathbf{x}) = \{1, x_1, x_2, x_1^2, x_1 x_2, x_2^2\} \quad \text{for } m = 6$$

are linear and quadratic basis functions, respectively. The basis functions are not required to be polynomials. It is convenient to introduce $r^{-1/2}$ singularity for secondary fields at the crack tip vicinity for modeling of fracture problems [15].

Then, the basis functions can be considered in the following form

$$\mathbf{p}^T(\mathbf{x}) = \{1, x_1, x_2, \sqrt{r} \cos(\theta/2), \sqrt{r} \sin(\theta/2), \sqrt{r} \sin(\theta/2) \sin \theta, \sqrt{r} \cos(\theta/2) \sin \theta\} \quad \text{for } m = 7,$$

where r and θ are polar coordinates with the crack tip as the origin.

The approximated functions for the Laplace transforms of the mechanical displacements, the electric and magnetic potentials can be written as [2]

$$\begin{aligned} \bar{\mathbf{u}}^h(\mathbf{x}, p) &= \Phi^T(\mathbf{x}) \cdot \hat{\mathbf{u}} = \sum_{a=1}^n \phi^a(\mathbf{x}) \hat{\mathbf{u}}^a(p), \\ \bar{\psi}^h(\mathbf{x}, p) &= \sum_{a=1}^n \phi^a(\mathbf{x}) \hat{\psi}^a(p), \\ \bar{\mu}^h(\mathbf{x}, p) &= \sum_{a=1}^n \phi^a(\mathbf{x}) \hat{\mu}^a(p), \end{aligned} \quad (20)$$

where the nodal values $\hat{\mathbf{u}}^a(p) = (\hat{u}_1^a(p), \hat{u}_3^a(p))^T$, $\hat{\psi}^a(p)$ and $\hat{\mu}^a(p)$ are fictitious parameters for the displacements, the electric and magnetic potentials, respectively, and $\phi^a(\mathbf{x})$ is the shape function associated with the node a . The number of nodes n used for the approximation is determined by the weight function $w^a(\mathbf{x})$. A 4th order spline-type weight function is applied in the present work

$$w^a(\mathbf{x}) = \begin{cases} 1 - 6 \left(\frac{d^a}{r^a}\right)^2 + 8 \left(\frac{d^a}{r^a}\right)^3 - 3 \left(\frac{d^a}{r^a}\right)^4, & 0 \leq d^a \leq r^a, \\ 0, & d^a \geq r^a, \end{cases} \quad (21)$$

where $d^a = \|\mathbf{x} - \mathbf{x}^a\|$ and r^a is the size of the support domain. It is seen that the C^1 -continuity is ensured over the entire domain, and therefore the continuity conditions of the tractions, the electric charge and the magnetic flux are satisfied.

The Laplace transform of traction vectors $\bar{t}_i(\mathbf{x}, p)$ at a boundary point $\mathbf{x} \in \partial\Omega_s$ are approximated in terms of the same nodal values $\hat{\mathbf{u}}^a(p)$ as

$$\begin{aligned} \bar{\mathbf{t}}^h(\mathbf{x}, p) &= \mathbf{N}(\mathbf{x}) \mathbf{C}(\mathbf{x}) \sum_{a=1}^n \mathbf{B}^a(\mathbf{x}) \hat{\mathbf{u}}^a(p) \\ &\quad + \mathbf{N}(\mathbf{x}) \mathbf{L}(\mathbf{x}) \sum_{a=1}^n \mathbf{P}^a(\mathbf{x}) \hat{\psi}^a(p) \\ &\quad + \mathbf{N}(\mathbf{x}) \mathbf{K}(\mathbf{x}) \sum_{a=1}^n \mathbf{P}^a(\mathbf{x}) \hat{\mu}^a(p), \end{aligned} \quad (22)$$

where the matrices $\mathbf{C}(\mathbf{x})$, $\mathbf{L}(\mathbf{x})$, and $\mathbf{K}(\mathbf{x})$ are defined in Eq. (10), the matrix $\mathbf{N}(\mathbf{x})$ is related to the normal vector

$\mathbf{n}(\mathbf{x})$ on $\partial\Omega_s$ by

$$\mathbf{N}(\mathbf{x}) = \begin{bmatrix} n_1 & 0 & n_3 \\ 0 & n_3 & n_1 \end{bmatrix}$$

and finally, the matrices \mathbf{B}^a and \mathbf{P}^a are represented by the gradients of the shape functions as

$$\mathbf{B}^a(\mathbf{x}) = \begin{bmatrix} \phi_{,1}^a & 0 \\ 0 & \phi_{,3}^a \\ \phi_{,3}^a & \phi_{,1}^a \end{bmatrix}, \quad \mathbf{P}^a(\mathbf{x}) = \begin{bmatrix} \phi_{,1}^a \\ \phi_{,3}^a \end{bmatrix}.$$

Similarly the Laplace-transform of the normal component of the electric displacement vector $\bar{Q}(\mathbf{x}, p)$ can be approximated by

$$\begin{aligned} \bar{Q}^h(\mathbf{x}, p) &= \mathbf{N}_1(\mathbf{x})\mathbf{G}(\mathbf{x}) \sum_{a=1}^n \mathbf{B}^a(\mathbf{x})\hat{\mathbf{u}}^a(p) \\ &\quad - \mathbf{N}_1(\mathbf{x})\mathbf{H}(\mathbf{x}) \sum_{a=1}^n \mathbf{P}^a(\mathbf{x})\hat{\psi}^a(p) \\ &\quad - \mathbf{N}_1(\mathbf{x})\mathbf{A}(\mathbf{x}) \sum_{a=1}^n \mathbf{P}^a(\mathbf{x})\hat{\mu}^a(p), \end{aligned} \quad (23)$$

where the matrices $\mathbf{G}(\mathbf{x})$, $\mathbf{H}(\mathbf{x})$, and $\mathbf{A}(\mathbf{x})$ are defined in Eq. (11) and

$$\mathbf{N}_1(\mathbf{x}) = [n_1 \quad n_3].$$

Eventually, the Laplace-transform of the magnetic flux $\bar{S}(\mathbf{x}, p)$ is approximated by

$$\begin{aligned} \bar{S}^h(\mathbf{x}, p) &= \mathbf{N}_1(\mathbf{x})\mathbf{R}(\mathbf{x}) \sum_{a=1}^n \mathbf{B}^a(\mathbf{x})\hat{\mathbf{u}}^a(p) \\ &\quad - \mathbf{N}_1(\mathbf{x})\mathbf{A}(\mathbf{x}) \sum_{a=1}^n \mathbf{P}^a(\mathbf{x})\hat{\psi}^a(p) \\ &\quad - \mathbf{N}_1(\mathbf{x})\mathbf{M}(\mathbf{x}) \sum_{a=1}^n \mathbf{P}^a(\mathbf{x})\hat{\mu}^a(p), \end{aligned} \quad (24)$$

with the matrices $\mathbf{R}(\mathbf{x})$ and $\mathbf{M}(\mathbf{x})$ being defined in Eq. (12).

Obeying the essential boundary conditions and making use of the approximation formula (20), one obtains the discretized form of these boundary conditions as

$$\begin{aligned} \sum_{a=1}^n \phi^a(\boldsymbol{\zeta})\hat{\mathbf{u}}^a(p) &= \tilde{\mathbf{u}}(\boldsymbol{\zeta}, p) \quad \text{for } \boldsymbol{\zeta} \in \Gamma_u, \\ \sum_{a=1}^n \phi^a(\boldsymbol{\zeta})\hat{\psi}^a(p) &= \tilde{\psi}(\boldsymbol{\zeta}, p) \quad \text{for } \boldsymbol{\zeta} \in \Gamma_p, \\ \sum_{a=1}^n \phi^a(\boldsymbol{\zeta})\hat{\mu}^a(p) &= \tilde{\mu}(\boldsymbol{\zeta}, p) \quad \text{for } \boldsymbol{\zeta} \in \Gamma_a. \end{aligned} \quad (25)$$

Furthermore, in view of the MLS-approximation (22)–(24) for the unknown quantities in the local boundary-domain

integral equations (16), (18) and (19), we obtain their discretized forms as

$$\begin{aligned} &\sum_{a=1}^n \left(\int_{L_s+\Gamma_{st}} \mathbf{N}(\mathbf{x})\mathbf{C}(\mathbf{x})\mathbf{B}^a(\mathbf{x})d\Gamma - \mathbf{I}\rho p^2 \int_{\Omega_s} \phi^a(\mathbf{x})d\Omega \right) \hat{\mathbf{u}}^a(p) \\ &\quad + \sum_{a=1}^n \left(\int_{L_s+\Gamma_{sq}} \mathbf{N}(\mathbf{x})\mathbf{L}(\mathbf{x})\mathbf{P}^a(\mathbf{x})d\Gamma \right) \hat{\psi}^a(p) \\ &\quad + \sum_{a=1}^n \left(\int_{L_s+\Gamma_{sb}} \mathbf{N}(\mathbf{x})\mathbf{K}(\mathbf{x})\mathbf{P}^a(\mathbf{x})d\Gamma \right) \hat{\mu}^a(p) \\ &= - \int_{\Gamma_{st}} \tilde{\mathbf{t}}(\mathbf{x}, p)d\Gamma - \int_{\Omega_s} \tilde{\mathbf{F}}(\mathbf{x}, p)d\Omega, \end{aligned} \quad (26)$$

$$\begin{aligned} &\sum_{a=1}^n \left(\int_{L_s+\Gamma_{sp}} \mathbf{N}_1(\mathbf{x})\mathbf{G}(\mathbf{x})\mathbf{B}^a(\mathbf{x})d\Gamma \right) \hat{\mathbf{u}}^a(p) \\ &\quad - \sum_{a=1}^n \left(\int_{L_s+\Gamma_{sp}} \mathbf{N}_1(\mathbf{x})\mathbf{H}(\mathbf{x})\mathbf{P}^a(\mathbf{x})d\Gamma \right) \hat{\psi}^a(p) \\ &\quad - \sum_{a=1}^n \left(\int_{L_s+\Gamma_{sp}} \mathbf{N}_1(\mathbf{x})\mathbf{A}(\mathbf{x})\mathbf{P}^a(\mathbf{x})d\Gamma \right) \hat{\mu}^a(p) \\ &= - \int_{\Gamma_{sq}} \tilde{Q}(\mathbf{x}, p)d\Gamma, \end{aligned} \quad (27)$$

$$\begin{aligned} &\sum_{a=1}^n \left(\int_{L_s+\Gamma_{sp}} \mathbf{N}_1(\mathbf{x})\mathbf{R}(\mathbf{x})\mathbf{B}^a(\mathbf{x})d\Gamma \right) \hat{\mathbf{u}}^a(p) \\ &\quad - \sum_{a=1}^n \left(\int_{L_s+\Gamma_{sp}} \mathbf{N}_1(\mathbf{x})\mathbf{A}(\mathbf{x})\mathbf{P}^a(\mathbf{x})d\Gamma \right) \hat{\psi}^a(p) \\ &\quad - \sum_{a=1}^n \left(\int_{L_s+\Gamma_{sp}} \mathbf{N}_1(\mathbf{x})\mathbf{M}(\mathbf{x})\mathbf{P}^a(\mathbf{x})d\Gamma \right) \hat{\mu}^a(p) \\ &= - \int_{\Gamma_{sq}} \tilde{S}(\mathbf{x}, p)d\Gamma, \end{aligned} \quad (28)$$

which are considered on the sub-domains adjacent to the interior nodes as well as to the boundary nodes on Γ_{st} , Γ_{sq} and Γ_{sb} . In Eq. (26), \mathbf{I} is a unit matrix defined by

$$\mathbf{I} = \begin{pmatrix} 1 & 0 \\ 0 & 1 \end{pmatrix}.$$

Collecting the discretized local boundary-domain integral equations together with the discretized boundary conditions

for the displacements, the electrical and magnetic potentials results in the complete system of linear algebraic equations for the computation of the nodal unknowns, namely, the Laplace-transforms of the fictitious parameters $\hat{\mathbf{u}}^a(p)$, $\hat{\psi}^a(p)$ and $\hat{\mu}^a(p)$. The time dependent values of the transformed quantities can be obtained by an inverse Laplace-transform. In the present analysis, the Stehfest's inversion algorithm [37] is used. If $\bar{f}(s)$ is the Laplace-transform of $f(t)$, an approximate value f_a of $f(t)$ for a specific time t is given by

$$f_a(t) = \frac{\ln 2}{t} \sum_{i=1}^N v_i \bar{f}\left(\frac{\ln 2}{t} i\right), \quad (29)$$

where

$$v_i = (-1)^{N/2+i} \sum_{k=[(i+1)/2]}^{\min(i, N/2)} \frac{k^{N/2}(2k)!}{(N/2-k)! k! (k-1)! (i-k)! (2k-i)!}. \quad (30)$$

In numerical analyses, we have considered $N = 10$ for single precision arithmetic. It means that for each time t we need to solve N boundary value problems for the corresponding Laplace-transform parameters $s = i \ln 2/t$, with $i = 1, 2, \dots, N$. If M denotes the number of the time instants in which we are interested to know $f(t)$, the number of the Laplace-transform solutions $\bar{f}(s_j)$ is then $M \times N$. It should be noted that the present computational method can be easily reformulated into real time formulation as it was shown recently for heat conduction problems in functionally graded materials [34]. It is shown there that accuracies in both Laplace transformed and real time formulations are similar.

3 Local boundary integral equations for 3-D axisymmetric problems

Let us consider a 3-D axisymmetric magneto-electro-elastic body generated by the rotation of the planar domain Ω bounded by the boundary Γ around the axis of symmetry as depicted in Fig. 1. Let us consider solids with hexagonal symmetry and the z -axis being oriented in the poling direction. Moreover, we assume the body to be transversely isotropic, i.e., the additional symmetry is the rotational symmetry with respect to the z -axis. For axisymmetric problems it is convenient to use cylindrical coordinates $\mathbf{x} \equiv (r, \varphi, z)$. Owing to the hexagonal symmetry, the tensors of material coefficients are the same as in the previous section and their cylindrical components can be identified with the Cartesian ones by equating the indices as $(r, \varphi, z) = (1, 2, 3)$ in the axial plane $(x_1, x_3) = (r, z)$. Furthermore, the angular component of the

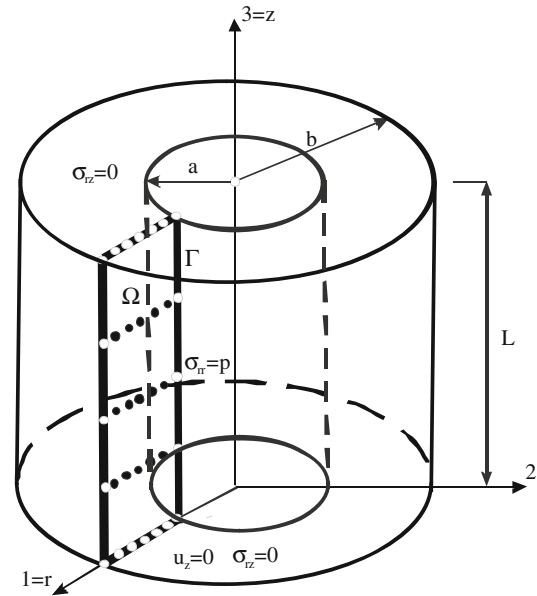


Fig. 1 A 3-D axisymmetric body

displacements vanishes and all physical field quantities are independent on the angular coordinate φ because of the axial symmetry. Thus, in the cylindrical coordinates also with the representation of tensors being with respect to the cylindrical unit basis vectors, the nonzero strains are given as

$$\varepsilon_{rr} = u_{r,r}, \quad \varepsilon_{\varphi\varphi} = u_r/r, \quad \varepsilon_{rz} = (u_{r,z} + u_{z,r})/2, \quad \varepsilon_{zz} = u_{z,z},$$

and the nonzero electrical and magnetic fields are $E_a = -\psi_{,a}$, $H_a = -\mu_{,a}$ with $a \in \{r, z\}$.

Thus, selecting the considered planar domain Ω in the axial plane $(x_1, x_3) = (r, z)$, we can apply the constitutive equations valid for crystals exhibiting hexagonal to nonzero components of the fields $\{\varepsilon_{ab}, E_a, H_a\}$ [30]. Then bearing in mind $c_{22} = c_{11}$, $c_{23} = c_{13}$, etc, we have

$$\begin{pmatrix} \sigma_{rr} \\ \sigma_{\varphi\varphi} \\ \sigma_{zz} \\ \sigma_{rz} \end{pmatrix} = \begin{bmatrix} c_{11} & c_{12} & c_{13} & 0 \\ c_{12} & c_{11} & c_{13} & 0 \\ c_{13} & c_{13} & c_{33} & 0 \\ 0 & 0 & 0 & c_{44} \end{bmatrix} \begin{pmatrix} u_{r,r} \\ u_r/r \\ u_{z,z} \\ u_{r,z} + u_{z,r} \end{pmatrix} - \begin{bmatrix} 0 & e_{31} \\ 0 & e_{31} \\ 0 & e_{33} \\ e_{15} & 0 \end{bmatrix} \begin{pmatrix} E_r \\ E_z \end{pmatrix} - \begin{bmatrix} 0 & d_{31} \\ 0 & d_{31} \\ 0 & d_{33} \\ d_{15} & 0 \end{bmatrix} \begin{pmatrix} H_r \\ H_z \end{pmatrix},$$

$$\begin{pmatrix} D_r \\ D_z \end{pmatrix} = \begin{bmatrix} 0 & 0 & 0 & e_{15} \\ e_{31} & e_{31} & e_{33} & 0 \end{bmatrix} \begin{pmatrix} u_{r,r} \\ u_r/r \\ u_{z,z} \\ u_{r,z} + u_{z,r} \end{pmatrix} + \begin{bmatrix} h_{11} & 0 \\ 0 & h_{33} \end{bmatrix} \begin{pmatrix} E_r \\ E_z \end{pmatrix} + \begin{bmatrix} \alpha_{11} & 0 \\ 0 & \alpha_{33} \end{bmatrix} \begin{pmatrix} H_r \\ H_z \end{pmatrix},$$

$$\begin{pmatrix} B_r \\ B_z \end{pmatrix} = \begin{bmatrix} 0 & 0 & 0 & d_{15} \\ d_{31} & d_{31} & d_{33} & 0 \end{bmatrix} \begin{pmatrix} u_{r,r} \\ u_r/r \\ u_{z,z} \\ u_{r,z} + u_{z,r} \end{pmatrix} + \begin{bmatrix} \alpha_{11} & 0 \\ 0 & \alpha_{33} \end{bmatrix} \begin{pmatrix} E_r \\ E_z \end{pmatrix} + \begin{bmatrix} \gamma_{11} & 0 \\ 0 & \gamma_{33} \end{bmatrix} \begin{pmatrix} H_r \\ H_z \end{pmatrix}. \quad (31)$$

In the cylindrical coordinate system, the governing equations (1), (2) and (5) take the form

$$\begin{aligned} & \sigma_{rr,r}(r, z, \tau) + \sigma_{rz,z}(r, z, \tau) + \frac{1}{r} [\sigma_{rr}(r, z, \tau) - \sigma_{\varphi\varphi}(r, z, \tau)] \\ & - \rho(\mathbf{x}) \ddot{u}_r(r, z, \tau) = -X_r(r, z, \tau), \\ & \sigma_{rz,r}(r, z, \tau) + \sigma_{zz,z}(r, z, \tau) + \frac{1}{r} \sigma_{rz}(r, z, \tau) \\ & - \rho(\mathbf{x}) \ddot{u}_z(r, z, \tau) = -X_z(r, z, \tau), \\ & D_{r,r}(r, z, \tau) + D_{z,z}(r, z, \tau) + \frac{1}{r} D_r(r, z, \tau) = 0, \\ & B_{r,r}(r, z, \tau) + B_{z,z}(r, z, \tau) + \frac{1}{r} B_r(r, z, \tau) = 0, \end{aligned} \quad (32)$$

Note that $c_{12} \neq c_{11}$ (and consequently $\sigma_{rr} - \sigma_{\varphi\varphi} \neq 0$) even in the case of the axial symmetry. The opposite has been assumed implicitly in Eqs. (3.28) and (3.29) of the book [30].

In the present analysis, all material parameters in the constitutive equations (31) are considered to be dependent on the (r, z) -coordinates.

Applying the Laplace transform to the first two equations in (32), we get

$$\begin{aligned} & \bar{\sigma}_{rr,r}(r, z, p) + \bar{\sigma}_{rz,z}(r, z, p) + \frac{1}{r} [\bar{\sigma}_{rr}(r, z, p) - \bar{\sigma}_{\varphi\varphi}(r, z, p)] \\ & - \rho(\mathbf{x}) p^2 \bar{u}_r(r, z, p) = -\bar{F}_r(r, z, p), \\ & \bar{\sigma}_{rz,r}(r, z, p) + \bar{\sigma}_{zz,z}(r, z, p) + \frac{1}{r} \bar{\sigma}_{rz}(r, z, p) \\ & - \rho(\mathbf{x}) p^2 \bar{u}_z(r, z, p) = -\bar{F}_z(r, z, p). \end{aligned} \quad (33)$$

Recall that the third and fourth equations in (32) remain unchanged by the Laplace transformation, i.e.,

$$\begin{aligned} & \bar{D}_{r,r}(r, z, p) + \bar{D}_{z,z}(r, z, p) + \frac{1}{r} \bar{D}_r(r, z, p) = 0, \\ & \bar{B}_{r,r}(r, z, p) + \bar{B}_{z,z}(r, z, p) + \frac{1}{r} \bar{B}_r(r, z, p) = 0. \end{aligned} \quad (34)$$

In numerical solution, we apply again the MLPG method to construct the weak form over local subdomains such as Ω_s , which is a small region taken for each node inside the global domain Ω . The local subdomains overlap each other, and cover the whole global domain Ω . The local subdomains could be of any geometric shape and size. In the present paper, the local subdomains are taken to be of circular shape.

The local weak forms of the governing equations (33) and (34) can be written as

$$\begin{aligned} & \int_{\Omega_s} (\bar{\sigma}_{rr,r} + \bar{\sigma}_{rz,z}) u^* d\Omega + \int_{\Omega_s} \frac{1}{r} (\bar{\sigma}_{rr} - \bar{\sigma}_{\varphi\varphi}) u^* d\Omega \\ & - \int_{\Omega_s} \rho(\mathbf{x}) p^2 \bar{u}_r(r, z, p) u^* d\Omega = - \int_{\Omega_s} \bar{F}_r(r, z, p) u^* d\Omega, \\ & \int_{\Omega_s} (\bar{\sigma}_{rz,r} + \bar{\sigma}_{zz,z}) v^* d\Omega + \int_{\Omega_s} \frac{1}{r} \bar{\sigma}_{rz}(r, z, p) v^* d\Omega \\ & - \int_{\Omega_s} \rho(\mathbf{x}) p^2 \bar{u}_z(r, z, p) v^* d\Omega = - \int_{\Omega_s} \bar{F}_z(r, z, p) v^* d\Omega, \\ & \int_{\Omega_s} (\bar{D}_{r,r} + \bar{D}_{z,z}) m^* d\Omega + \int_{\Omega_s} \frac{1}{r} \bar{D}_r(r, z, p) m^* d\Omega = 0, \\ & \int_{\Omega_s} (\bar{B}_{r,r} + \bar{B}_{z,z}) \beta^* d\Omega + \int_{\Omega_s} \frac{1}{r} \bar{B}_r(r, z, p) \beta^* d\Omega = 0, \end{aligned} \quad (35)$$

where $u^*(\mathbf{x})$, $v^*(\mathbf{x})$, $m^*(\mathbf{x})$ and $\beta^*(\mathbf{x})$ are test functions.

Applying the Gauss divergence theorem to the first domain integrals of Eqs. (35) and selecting Heaviside unit step functions as test functions $u^*(\mathbf{x})$, $v^*(\mathbf{x})$, $m^*(\mathbf{x})$ and $\beta^*(\mathbf{x})$ in each subdomain, one can recast these equations into the following forms

$$\begin{aligned} & \int_{\partial\Omega_s} \bar{\sigma}_{rb}(r, z, p) n_b d\Gamma + \int_{\Omega_s} \frac{1}{r} (\bar{\sigma}_{rr} - \bar{\sigma}_{\varphi\varphi}) d\Omega \\ & - \int_{\Omega_s} \rho(\mathbf{x}) p^2 \bar{u}_r(r, z, p) d\Omega = - \int_{\Omega_s} \bar{F}_r(r, z, p) d\Omega, \\ & \int_{\partial\Omega_s} \bar{\sigma}_{zb}(r, z, p) n_b d\Gamma + \int_{\Omega_s} \frac{1}{r} \bar{\sigma}_{rz}(r, z, p) d\Omega \\ & - \int_{\Omega_s} \rho(\mathbf{x}) p^2 \bar{u}_z(r, z, p) d\Omega = - \int_{\Omega_s} \bar{F}_z(r, z, p) d\Omega, \\ & \int_{\partial\Omega_s} \bar{D}_b(r, z, p) n_b d\Gamma + \int_{\Omega_s} \frac{1}{r} \bar{D}_r(r, z, p) d\Omega = 0, \\ & \int_{\partial\Omega_s} \bar{B}_b(r, z, p) n_b d\Gamma + \int_{\Omega_s} \frac{1}{r} \bar{B}_r(r, z, p) d\Omega = 0, \end{aligned} \quad (36)$$

where the subscript b in Eq. (36) is considered as a summation index with $b = r, z$.

As in 2-D problems the displacement and the potential fields are approximated by the MLS approximation. Substituting the approximation formula (20) into the LIEs (36) a system of linear algebraic equations for the unknown fictitious parameters $\{\hat{u}_r^a, \hat{u}_z^a, \hat{\psi}^a, \hat{\mu}^a\}$ is obtained as

$$\begin{aligned}
 & \sum_{a=1}^n \hat{u}_r^a(p) \left\{ \int_{\partial\Omega_s} \left[c_{11}(\mathbf{x}) n_r(\mathbf{x}) \phi_{,r}^a(\mathbf{x}) + \frac{c_{12}(\mathbf{x})}{r} n_r(\mathbf{x}) \phi^a(\mathbf{x}) \right. \right. \\
 & \quad \left. \left. + d_{33}(\mathbf{x}) n_z(\mathbf{x}) \phi_{,z}^a(\mathbf{x}) \right] d\Gamma + \int_{\Omega_s} \frac{1}{r} d_{15}(\mathbf{x}) \phi_{,r}^a(\mathbf{x}) d\Omega \right\} \\
 & \quad + c_{44}(\mathbf{x}) n_z(\mathbf{x}) \phi_{,z}^a(\mathbf{x}) \Big] d\Gamma + \int_{\Omega_s} \left[\frac{1}{r} (c_{11}(\mathbf{x}) \right. \\
 & \quad \left. - c_{12}(\mathbf{x})) \left(\phi_{,r}^a(\mathbf{x}) - \frac{1}{r} \phi^a(\mathbf{x}) \right) - \rho(\mathbf{x}) p^2 \phi^a(\mathbf{x}) \right] d\Omega \Big\} \\
 & \quad + \sum_{a=1}^n \hat{u}_z^a(p) \int_{\partial\Omega_s} (c_{13}(\mathbf{x}) n_r(\mathbf{x}) \phi_{,z}^a(\mathbf{x}) + c_{44}(\mathbf{x}) n_z(\mathbf{x}) \\
 & \quad \times \phi_{,r}^a(\mathbf{x})) d\Gamma + \sum_{a=1}^n \hat{\psi}^a(p) \int_{\partial\Omega_s} (e_{31}(\mathbf{x}) n_r(\mathbf{x}) \phi_{,z}^a(\mathbf{x}) \\
 & \quad + e_{15}(\mathbf{x}) n_z(\mathbf{x}) \phi_{,r}^a(\mathbf{x})) d\Gamma + \sum_{a=1}^n \hat{\mu}^a(p) \int_{\partial\Omega_s} (d_{31}(\mathbf{x}) n_r(\mathbf{x}) \\
 & \quad \times \phi_{,z}^a(\mathbf{x}) + d_{15}(\mathbf{x}) n_z(\mathbf{x}) \phi_{,r}^a(\mathbf{x})) d\Gamma \\
 & = - \int_{\Omega_s} \bar{F}_r(r, z, p) d\Omega, \tag{37}
 \end{aligned}$$

$$\begin{aligned}
 & \sum_{a=1}^n \hat{u}_z^a(p) \left\{ \int_{\partial\Omega_s} [c_{33}(\mathbf{x}) n_z(\mathbf{x}) \phi_{,z}^a(\mathbf{x}) + c_{44}(\mathbf{x}) n_r(\mathbf{x}) \phi_{,r}^a(\mathbf{x})] d\Gamma \right. \\
 & \quad \left. + \int_{\Omega_s} \left[\frac{c_{44}(\mathbf{x})}{r} \phi_{,r}^a(\mathbf{x}) - \rho(\mathbf{x}) p^2 \phi^a(\mathbf{x}) \right] d\Omega \right\} \\
 & \quad + \sum_{a=1}^n \hat{u}_r^a(p) \left\{ \int_{\partial\Omega_s} (c_{44}(\mathbf{x}) n_r(\mathbf{x}) \phi_{,z}^a(\mathbf{x}) + c_{13}(\mathbf{x}) n_z(\mathbf{x}) \right. \\
 & \quad \times (\phi_{,r}^a(\mathbf{x}) + \frac{1}{r} \phi^a(\mathbf{x}))) d\Gamma + \int_{\Omega_s} \frac{c_{44}(\mathbf{x})}{r} \phi_{,z}^a(\mathbf{x}) d\Omega \Big\} \\
 & \quad + \sum_{a=1}^n \hat{\psi}^a(p) \left\{ \int_{\partial\Omega_s} (e_{15}(\mathbf{x}) n_r(\mathbf{x}) \phi_{,r}^a(\mathbf{x}) + e_{33}(\mathbf{x}) n_z(\mathbf{x}) \right. \\
 & \quad \times \phi_{,z}^a(\mathbf{x})) d\Gamma + \int_{\Omega_s} \frac{1}{r} e_{15}(\mathbf{x}) \phi_{,r}^a(\mathbf{x}) d\Omega \Big\} \\
 & \quad + \sum_{a=1}^n \hat{\mu}^a(p) \left\{ \int_{\partial\Omega_s} (d_{15}(\mathbf{x}) n_r(\mathbf{x}) \phi_{,r}^a(\mathbf{x}) \right. \\
 & \quad \left. + h_{33}(\mathbf{x}) n_z(\mathbf{x}) \phi_{,z}^a(\mathbf{x})) d\Gamma + \int_{\Omega_s} \frac{1}{r} h_{11}(\mathbf{x}) \phi_{,r}^a(\mathbf{x}) d\Omega \right\} \\
 & \quad - \sum_{a=1}^n \hat{\mu}^a(p) \left\{ \int_{\partial\Omega_s} (\alpha_{11}(\mathbf{x}) n_r(\mathbf{x}) \phi_{,r}^a(\mathbf{x}) + \alpha_{33}(\mathbf{x}) n_z(\mathbf{x}) \right. \\
 & \quad \times \phi_{,z}^a(\mathbf{x})) d\Gamma + \int_{\Omega_s} \frac{1}{r} \alpha_{11}(\mathbf{x}) \phi_{,r}^a(\mathbf{x}) d\Omega \Big\} = 0, \tag{39}
 \end{aligned}$$

$$\begin{aligned}
 & \sum_{a=1}^n \hat{u}_r^a(p) \left\{ \int_{\partial\Omega_s} \left[e_{15}(\mathbf{x}) n_r(\mathbf{x}) \phi_{,z}^a(\mathbf{x}) + e_{31}(\mathbf{x}) n_z(\mathbf{x}) \right. \right. \\
 & \quad \times \left(\phi_{,r}^a(\mathbf{x}) + \frac{1}{r} \phi^a(\mathbf{x}) \right) \Big] d\Gamma + \int_{\Omega_s} \frac{1}{r} e_{15}(\mathbf{x}) \phi_{,z}^a(\mathbf{x}) d\Omega \Big\} \\
 & \quad + \sum_{a=1}^n \hat{u}_z^a(p) \left\{ \int_{\partial\Omega_s} [e_{15}(\mathbf{x}) n_r(\mathbf{x}) \phi_{,r}^a(\mathbf{x}) + e_{33}(\mathbf{x}) n_z(\mathbf{x}) \right. \\
 & \quad \times \phi_{,z}^a(\mathbf{x})] d\Gamma + \int_{\Omega_s} \frac{1}{r} e_{15}(\mathbf{x}) \phi_{,r}^a(\mathbf{x}) d\Omega \Big\} \\
 & \quad - \sum_{a=1}^n \hat{\psi}^a(p) \left\{ \int_{\partial\Omega_s} (h_{11}(\mathbf{x}) n_r(\mathbf{x}) \phi_{,r}^a(\mathbf{x}) \right. \\
 & \quad \left. + h_{33}(\mathbf{x}) n_z(\mathbf{x}) \phi_{,z}^a(\mathbf{x})) d\Gamma + \int_{\Omega_s} \frac{1}{r} h_{11}(\mathbf{x}) \phi_{,r}^a(\mathbf{x}) d\Omega \right\} \\
 & \quad - \sum_{a=1}^n \hat{\mu}^a(p) \left\{ \int_{\partial\Omega_s} (\alpha_{11}(\mathbf{x}) n_r(\mathbf{x}) \phi_{,r}^a(\mathbf{x}) + \alpha_{33}(\mathbf{x}) n_z(\mathbf{x}) \right. \\
 & \quad \times \phi_{,z}^a(\mathbf{x})) d\Gamma + \int_{\Omega_s} \frac{1}{r} \alpha_{11}(\mathbf{x}) \phi_{,r}^a(\mathbf{x}) d\Omega \Big\} = 0, \tag{39}
 \end{aligned}$$

$$\begin{aligned}
 & \sum_{a=1}^n \hat{u}_r^a(p) \left\{ \int_{\partial\Omega_s} \left[d_{15}(\mathbf{x}) n_r(\mathbf{x}) \phi_{,z}^a(\mathbf{x}) + d_{31}(\mathbf{x}) n_z(\mathbf{x}) \right. \right. \\
 & \quad \times \left(\phi_{,r}^a(\mathbf{x}) + \frac{1}{r} \phi^a(\mathbf{x}) \right) \Big] d\Gamma + \int_{\Omega_s} \frac{1}{r} d_{15}(\mathbf{x}) \phi_{,z}^a(\mathbf{x}) d\Omega \Big\} \\
 & \quad + \sum_{a=1}^n \hat{u}_z^a(p) \left\{ \int_{\partial\Omega_s} [d_{15}(\mathbf{x}) n_r(\mathbf{x}) \phi_{,r}^a(\mathbf{x}) + d_{33}(\mathbf{x}) n_z(\mathbf{x}) \right. \\
 & \quad \times \phi_{,z}^a(\mathbf{x})] d\Gamma + \int_{\Omega_s} \frac{1}{r} d_{15}(\mathbf{x}) \phi_{,r}^a(\mathbf{x}) d\Omega \Big\}
 \end{aligned}$$

$$\begin{aligned}
& - \sum_{a=1}^n \hat{\psi}^a(p) \left\{ \int_{\partial\Omega_s} (\alpha_{11}(\mathbf{x}) n_r(\mathbf{x}) \phi_{,r}^a(\mathbf{x}) \right. \\
& \quad \left. + \alpha_{33}(\mathbf{x}) n_z(\mathbf{x}) \phi_{,z}^a(\mathbf{x}) d\Gamma + \int_{\Omega_s} \frac{1}{r} \alpha_{11}(\mathbf{x}) \phi_{,r}^a(\mathbf{x}) d\Omega \right\} \\
& - \sum_{a=1}^n \hat{\mu}^a(p) \left\{ \int_{\partial\Omega_s} (\gamma_{11}(\mathbf{x}) n_r(\mathbf{x}) \phi_{,r}^a(\mathbf{x}) \right. \\
& \quad \left. + \gamma_{33}(\mathbf{x}) n_z(\mathbf{x}) \phi_{,z}^a(\mathbf{x}) d\Gamma \right. \\
& \quad \left. + \int_{\Omega_s} \frac{1}{r} \gamma_{11}(\mathbf{x}) \phi_{,r}^a(\mathbf{x}) d\Omega \right\} = 0, \quad (40)
\end{aligned}$$

Equations (37)–(40) are considered in the subdomains Ω_s around each interior node \mathbf{x}^s and at boundary nodes with prescribed natural boundary conditions (Γ_t , Γ_q and Γ_b). On the parts of the global boundary Γ_u with prescribed elastic displacements, Γ_p with prescribed electric potentials and Γ_a with prescribed magnetic potential the collocation equations are applied like in 2-D problem.

4 Numerical examples

4.1 A central crack in a finite strip

In the first example, a straight central crack in a finite magneto-electro-elastic strip under a uniform pure mechanical and/or electro-magnetic loading is analyzed. The mechanical $\sigma_0 = 1$ Pa, electrical $D_0 = 1$ C/m² and magnetic induction $B_0 = 1$ Vs/m² loads are applied on the top side of the strip, respectively, in the static analysis. Each of the loads can open the crack and even to cause its propagation. Due to the bi-axial symmetry of the problem only a quarter of the cracked strip is modeled (Fig. 2). The cracked strip geometry values are: $a = 0.5$, $a/w = 0.4$ and $h/w = 1.2$. The mechanical displacements, the electrical and magnetic potentials on the finite strip are approximated by using 930 (31×30) equidistantly distributed nodes. The local subdomains are selected to be circular with a radius $r_{loc} = 0.028$ m. To test the accuracy of the present method homogeneous material properties are considered.

The material parameters corresponding to the BaTiO₃–CoFe₂O₄ composite are given by [23]

$$\begin{aligned}
c_{11} &= 22.6 \times 10^{10} \text{ Nm}^{-2}, & c_{13} &= 12.4 \times 10^{10} \text{ Nm}^{-2}, \\
c_{33} &= 21.6 \times 10^{10} \text{ Nm}^{-2}, & c_{66} &= 4.4 \times 10^{10} \text{ Nm}^{-2}, \\
e_{15} &= 5.8 \text{ Cm}^{-2}, & e_{31} &= -2.2 \text{ Cm}^{-2}, & e_{33} &= 9.3 \text{ Cm}^{-2}, \\
h_{11} &= 5.64 \times 10^{-9} \text{ C}^2/\text{Nm}^2, & h_{33} &= 6.35 \times 10^{-9} \text{ C}^2/\text{Nm}^2,
\end{aligned}$$

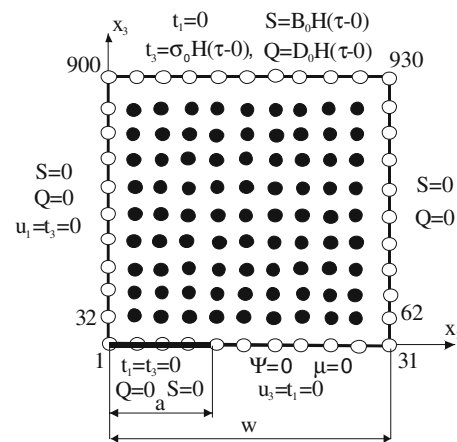


Fig. 2 A central crack in a finite magneto-electro-elastic strip

$$\begin{aligned}
d_{15} &= 275.0 \text{ N/Am}, & d_{21} &= 290.2 \text{ N/Am}, \\
d_{22} &= 350.0 \text{ N/Am}, \\
\alpha_{11} &= 5.367 \times 10^{-12} \text{ Ns/VC}, & \alpha_{33} &= 2737.5 \times 10^{-12} \text{ Ns/VC}, \\
\gamma_{11} &= 297.0 \times 10^{-6} \text{ Ns}^2\text{C}^{-2}, & \gamma_{33} &= 83.5 \times 10^{-6} \text{ Ns}^2\text{C}^{-2}, \\
\rho &= 5500 \text{ kg/m}^3.
\end{aligned}$$

For cracks in homogeneous and linear piezoelectric and piezomagnetic solids the asymptotic behavior of the field quantities has been given by Wang and Mai [44]. In the crack tip vicinity, the displacements and potentials show the classical \sqrt{r} asymptotic behavior. Hence, correspondingly, stresses, the electrical displacement and magnetic induction exhibit $1/\sqrt{r}$ behavior, where r is the radial polar coordinate with origin at the crack tip. Garcia-Sanchez et al. [17] extended the approach used in piezoelectricity to magneto-electroelasticity to obtain asymptotic expression of generalized intensity factors

$$\begin{pmatrix} K_{II} \\ K_I \\ K_E \\ K_M \end{pmatrix} = \sqrt{\frac{\pi}{2r}} [Re(\mathbf{B})^{-1}] \begin{pmatrix} u_1 \\ u_3 \\ \psi \\ \mu \end{pmatrix}, \quad (41)$$

where the matrix \mathbf{B} is determined by the material properties [17, 18] and

$$\begin{aligned}
K_I &= \lim_{r \rightarrow 0} \sqrt{2\pi r} \sigma_{33}(r, 0), \\
K_{II} &= \lim_{r \rightarrow 0} \sqrt{2\pi r} \sigma_{13}(r, 0), \\
K_E &= \lim_{r \rightarrow 0} \sqrt{2\pi r} D_3(r, 0), \\
K_M &= \lim_{r \rightarrow 0} \sqrt{2\pi r} B_3(r, 0),
\end{aligned}$$

are the SIF K_I and K_{II} , the EDIF, and the MIIF, respectively.

Enriched and conventional polynomial basis functions in the MLS approximation have been tested in Fig. 3. One can observe slight differences of crack opening displacements at

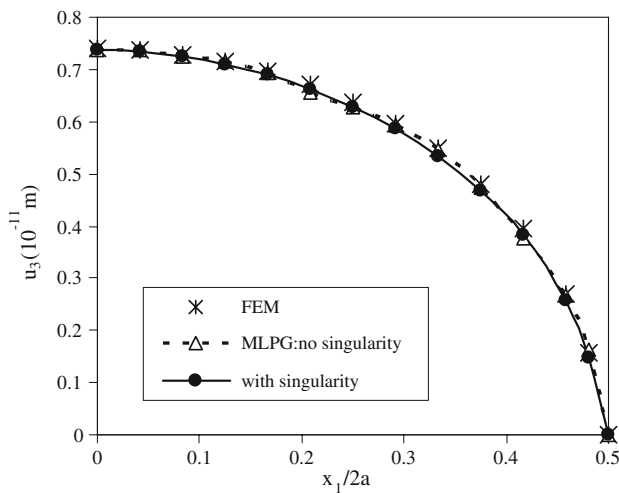


Fig. 3 Influence of modeling of singularities on the crack opening displacement under a pure mechanical loading σ_0 and impermeable conditions

the crack tip vicinity depending on whether the singularity of fields is considered or not. Quantities at the crack tip vicinity are important for an accurate evaluation of intensity factors from asymptotic expressions. Implementation of singular fields in meshless methods is substantially simple and trouble-free as compared to FEM [15].

If a crack in magneto-electro-elastic solids is investigated, an important question is how the medium inside the crack is modeled. Depending on the ratio between the dielectric permittivity and/or magnetic permeability of the medium inside the crack and that of the cracked solid, two extreme cases can be considered. In the first extreme case, the crack is not visible for the electric and/or magnetic field if the permittivity of the medium inside the crack is significantly larger than that of the analyzed solid. In such a case, the potentials on both crack-surfaces are the same, i.e., $\psi^+ = \psi^-$, $\mu^+ = \mu^-$, and thus one has the so-called electrically or magnetically permeable boundary conditions on the crack-surfaces:

$$D_n^+ = D_n^-, \quad B_n^+ = B_n^-.$$

In the second extreme case, the permittivity and permeability of the medium inside the crack are vanishing. Then, the electrical displacements and magnetic induction on both crack-surfaces are vanishing and potentials jump occurs.

$$D_n^+ = D_n^- = 0, \quad B_n^+ = B_n^- = 0.$$

This case corresponds to the so-called impermeable boundary conditions and they are shown in Fig. 2. One can observe from Fig. 4 that the crack opening displacements under stationary conditions are slightly larger under a pure mechanical load with permeable boundary conditions than that with the impermeable ones. However, the SIFs under a pure mechanical load is the same for both boundary conditions $K_I^{\text{stat}} =$

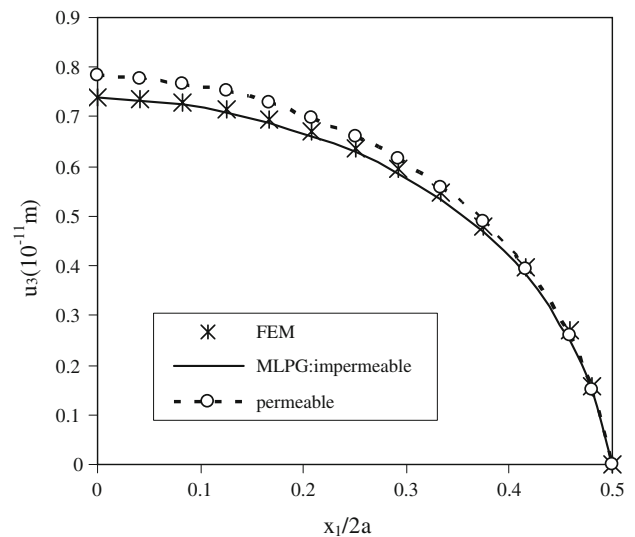


Fig. 4 Variation of the crack opening displacement with the normalized coordinate $x_1/2a$ under a pure mechanical loading σ_0

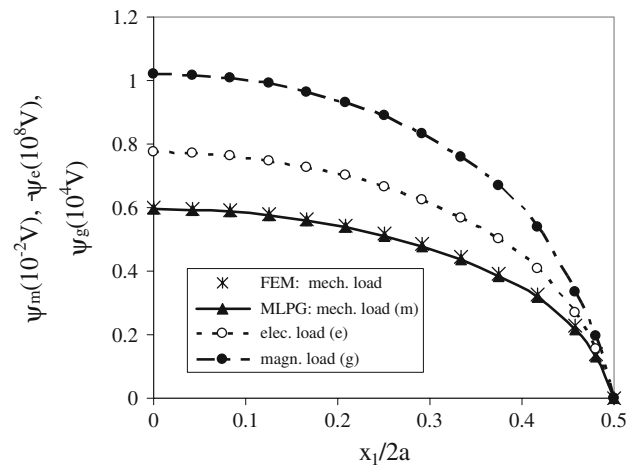


Fig. 5 Variation of electrical potentials with the normalized coordinate $x_1/2a$ under pure mechanical, electrical and magnetic loads, respectively

$1.4 \text{ Pa m}^{1/2}$. Enriched basis functions are applied in computation. Variation of the electrical and magnetic potentials corresponding to all three different loads along the crack is shown in Figs. 5 and 6, respectively. Impermeable boundary conditions are considered there, since both electrical and magnetic potentials are vanishing on the crack surfaces at permeable boundary conditions. The FEM results for the mechanical load are obtained by the ANSYS-code using 8037 quadratic (8-node) elements. A very fine FEM mesh is selected to obtain reliable results which are used as a benchmark. One can observe a good coincidence of the present and FEM results. Computational cost is 40% lower for the present method with 930 nodes than for FEM analysis with significantly higher number of elements. For comparable meshes

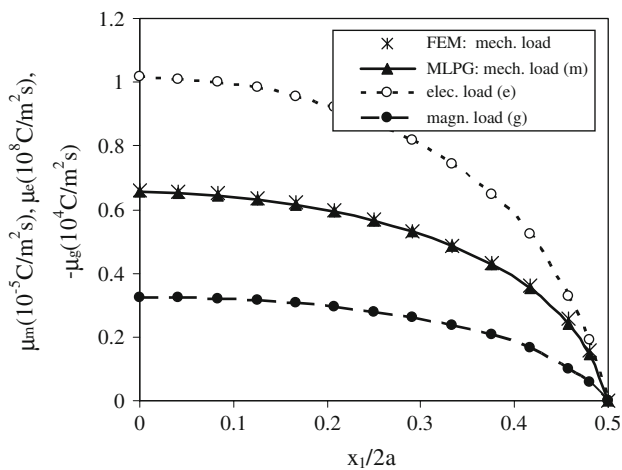


Fig. 6 Variation of magnetic potentials with the normalized coordinate $x_1/2a$ under pure mechanical, electrical and magnetic loads, respectively

in both methods the CPU in the present meshless method is 2.5 times longer than in a conventional discretization method with polynomial shape functions. This is due to a more complicated evaluation of shape functions at integration points in MLS approximation than in a classical polynomial approach. This phenomenon is observed at all meshless methods based on the MLS approximation. It is not caused by the selection of the test function in the weak form to derive the LIEs. The CPU in MLS approximations is influenced by the selection of the support domain size or the weight function. Smaller values of the support domain lead to lower approximation accuracy, and larger values of the support domain prolong the computational time for the evaluation of the shape functions. More detailed analyses on the influence of the support domain on computational accuracy can be found in Atluri [2]. To reduce the computing time, a mixed formulation [4] can be applied, which reduces the radius of the support domain at the same accuracy as in the traditional approximation. The other way is to use a new stabilized nodal integration approach [8] which also significantly reduces the CPU in techniques based on the MLS.

It is interesting to note that under a pure mechanical loading, finite values of the electrical and magnetic potentials on both crack surfaces do not result in a finite value of the EDIF or the MIIF. It means that the crack opening displacement u_3 and both the electrical, and magnetic potentials ψ_m , μ_m are coupled, but the SIF and both EDIF and MIIF in this case are uncoupled. The EDIF and MIIF are vanishing for a pure mechanical load under a static assumption.

Recently, we have analyzed the influence of combined mechanical and electrical loads on the SIF and EDIF in piezoelectric materials [34]. Here, we are interested in the influence of the magnetic induction due to the combined mechanical-magnetic load on the SIF and MIIF. For

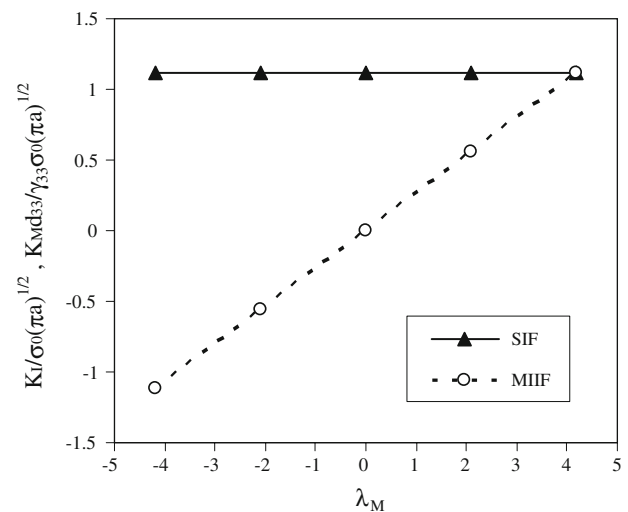


Fig. 7 Influence of the magnetic load on the stress intensity and magnetic induction intensity factors

convenience, a nondimensional loading parameter $\lambda_M = B_0 d_{33}/(\sigma_0 \gamma_{33})$ is introduced to quantify the intensity of the magnetic load. Variation of the normalized stress and MIIF with the applied magnetic induction load is presented in Fig. 7. Both positive and negative magnetic inductions are considered here. The intensity of the magnetic induction load has a neglected influence on the stress intensity factor. Uncoupling both intensity factors under a static assumption leads to a linear variation of the MIIF with increasing intensity of the magnetic load.

Next, the strip is subjected to an impact load with the Heaviside time variation and the intensity $\sigma_0 = 1$ Pa for a pure mechanical load and $B_0 = 1$ Vs/m² for a pure magnetic induction load, respectively. Both impermeable and permeable boundary conditions on the crack surfaces are considered. The time variation of the normalized stress intensity factor is given in Fig. 8. Both extreme boundary conditions on crack surfaces have a vanishing influence on the SIF for a pure mechanical load. The dynamic value of the SIF is approximately doubled as compared to the corresponding static one.

In Fig. 9a, b, we present the variation of the EDIF and MIIF under a pure mechanical load. On contrary to the static case a finite value for both intensity factors is predicted. From the Maxwell's equations, it is known that the velocity of electromagnetic waves is equal to the speed of light, which is much greater than the velocity of elastic waves. Hence, the use of quasi-static approximation in governing equations is justified for the interaction of electro-magnetic and mechanical fields. The response of the electro-magnetic fields is immediate, while that of the elastic ones is taken as finite because of the finite velocity of elastic waves. On the other hand, in a static case, the response of both the

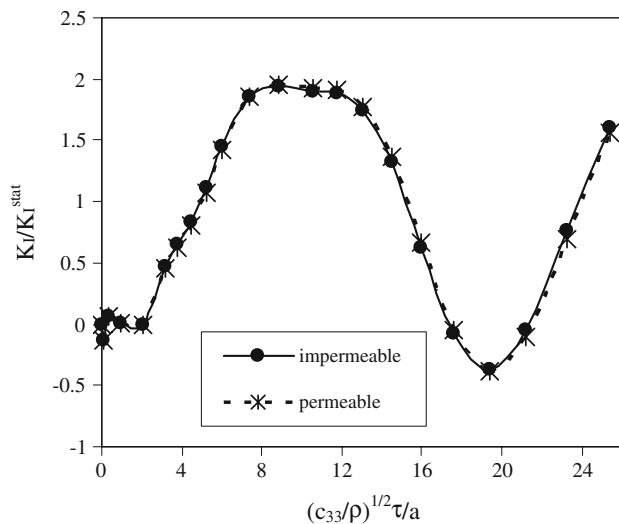


Fig. 8 Normalized stress intensity factor for a central crack in a strip under a pure mechanical load $\sigma_0 H(\tau - 0)$

mechanical (strains, stresses) and electro-magnetic fields is immediate. Thus, the SIF vanishes in such a case since the stresses σ_{33} are zero ahead of the crack tip on the crack line because of the immediate electro-magnetic–mechanical interaction. In the dynamic case the stress field is not only coupled to the immediate electro-magnetic field, but is also affected by the inertia forces.

For the normalized EDIF and MIIF in Fig. 9a,b we have used parameters $\Lambda_e = e_{33}/h_{33}$ and $\Lambda_m = d_{33}/\gamma_{33}$, respectively. The EDIF and MIIF are higher for permeable electro-magnetic boundary conditions than for the impermeable ones.

Figure 10 presents normalized stress and electrical intensity factors for a pure magnetic induction impact load. The static MIIF $K_M^{\text{stat}} = 1.4 \text{ Vsm}^{-3/2}$ has the same quantity as the static SIF for a pure mechanical load due to their decoupling. Both SIF and EDIF are oscillating around zero with high amplitude. Therefore, they have to be considered in design where transient processes are expected.

4.2 An edge crack in a finite strip

Next, an edge crack in a finite magneto-electric-elastic strip is analyzed. The geometry of the strip is given in Fig. 11 with the following values: $a = 0.5$, $a/w = 0.4$ and $h/w = 1.2$. Due to the symmetry of the problem with respect to the x_1 -axis, only a half of the strip is modeled. We have used again 930 equidistantly distributed nodes for the MLS approximation of the physical fields. On the top of the strip either a uniform tension σ_0 , or a uniform magnetic induction B_0 is applied. Firstly, the static loadings are considered. The functionally graded material properties in the x_1 -direction are considered. An exponential variation of the elastic, piezoelectric, dielec-

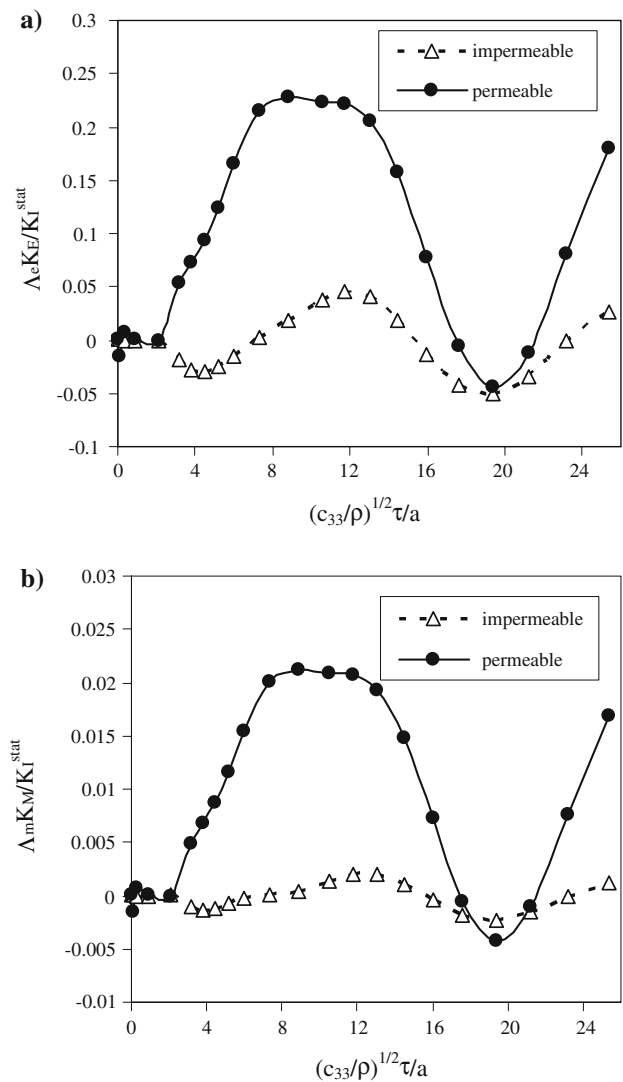


Fig. 9 Normalized **a** electric, and **b** magnetic intensity factors for a central crack in a strip under a pure mechanical load $\sigma_0 H(\tau - 0)$

tric, paramagnetic, electromagnetic and magnetic permeability coefficients are assumed as

$$f_{ij}(\mathbf{x}) = f_{ij0} \exp(\gamma x_1), \quad (42)$$

where the symbol f_{ij} is commonly used for partial material coefficients and f_{ij0} correspond to the material parameters used in the previous example. It should be noted that different exponential factor γ can be used for different material coefficients.

Figures 12 and 13 present the variation of the crack opening displacement and the electro-magnetic potentials on the crack surfaces with the x_1 -coordinate under a pure mechanical tension. We have considered the same exponential gradient for all coefficients with value $\gamma = 2$ in the numerical calculations. Then, all material parameters at the crack tip are $e^1 = 2.718$ times larger than in the homogeneous

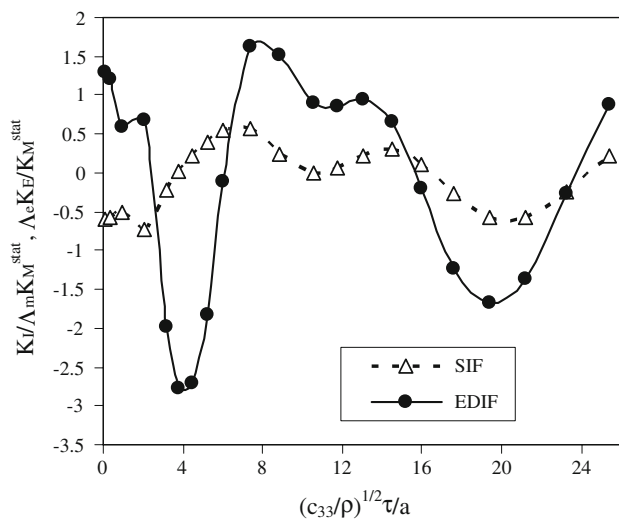


Fig. 10 Normalized stress and electric intensity factors for a central crack in a strip under a pure magnetic induction load $B_0 H (\tau = 0)$

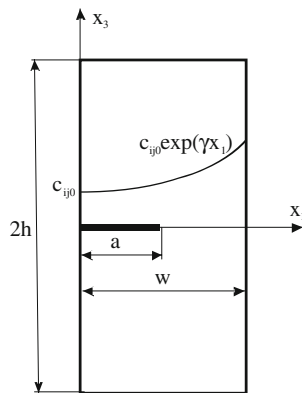


Fig. 11 An edge crack in a finite strip with graded material properties in x_1 -direction

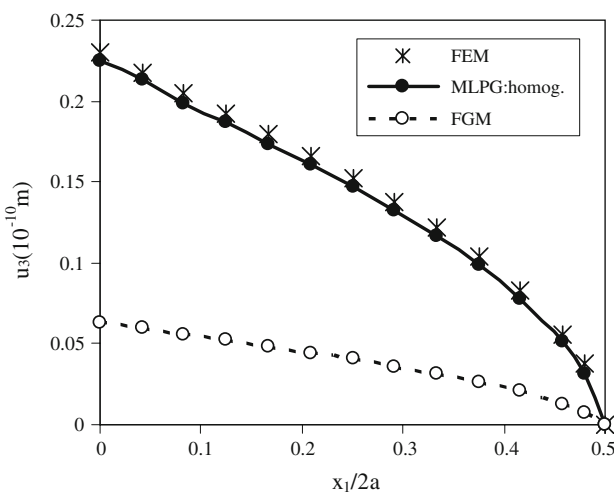


Fig. 12 Variation of the crack opening displacement with the normalized coordinate $x_1/2a$ under a pure mechanical loading $\sigma_0 = 1$ Pa

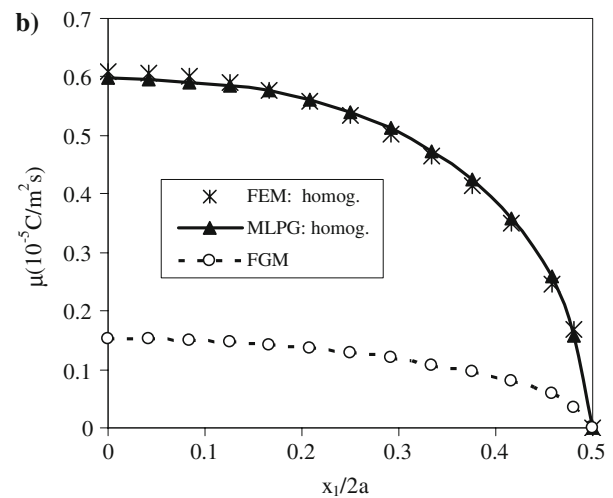
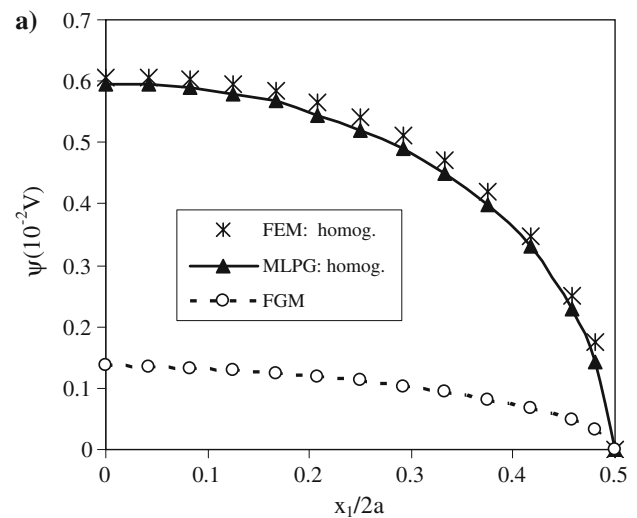


Fig. 13 Variation of **a** the electric, and **b** the magnetic potentials with the normalized coordinate $x_1/2a$ under a pure mechanical loading $\sigma_0 = 1$ Pa

material. One can see that the crack opening displacement and potentials are significantly reduced in the nonhomogeneous material with gradually increasing material properties in x_1 -direction. The boundary value problem for a homogeneous material has been analyzed also by the FEM computer code ANSYS. One can observe a quite good agreement for both results.

The normalized SIF for homogeneous and nonhomogeneous cracked specimen have the following values, $f_I = K_I / \sigma_0 \sqrt{\pi a} = 2.105$ and 1.565 , respectively. With increasing gradient parameter γ the SIF is decreasing. A similar phenomenon is observed for an edge crack in an elastic FGM strip under a mechanical loading [10] and for a cracked piezoelectric FGM specimen [35]. For a crack in a homogeneous magnet-electric-elastic solid analyzed in the previous example the SIF, EDIF, MIIF are uncoupled. However, this conclusion does not valid generally for a continuously

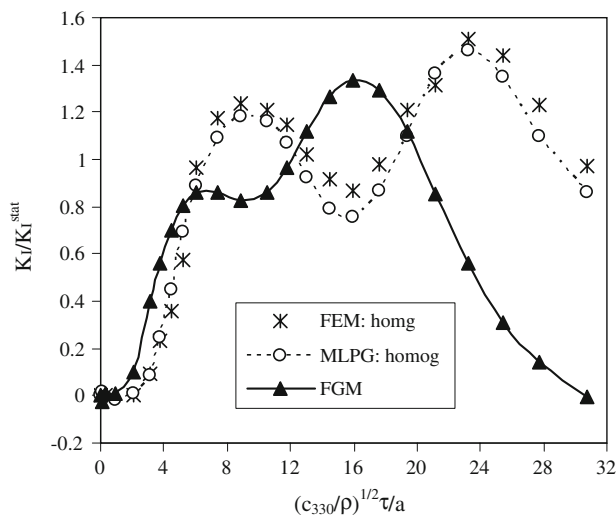


Fig. 14 Normalized stress intensity factor for an edge crack in a strip under a pure mechanical load $\sigma_0 H(\tau - 0)$

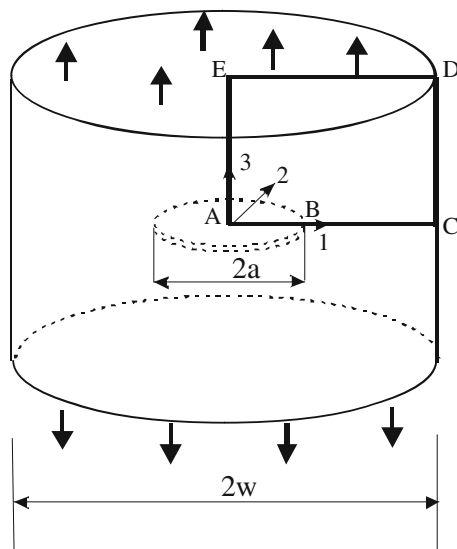


Fig. 15 A penny-shaped crack in a finite magneto-electro-elastic cylinder

nonhomogeneous solid. We have obtained the following normalized quantities: $\Lambda_e K_E / K_I^{\text{stat}} = 0.04866$ and $\Lambda_m K_M / K_I^{\text{stat}} = 0.00412$.

Next, the strip is subjected to an impact mechanical load with Heaviside time variation and the intensity $\sigma_0 = 1$ Pa. The impermeable boundary conditions for the electric displacement and magnetic flux on crack surfaces are considered. The time variation of the normalized stress intensity factor is given in Fig. 14, where $K_I^{\text{stat}} = 2.642 \text{ Pa m}^{1/2}$.

For a mechanical FGMs along the x_1 -coordinate and a uniform mass density, the wave propagation is growing with x_1 . Therefore, the peak value of the SIF is reached in a shorter time instant in functionally graded strip than in a

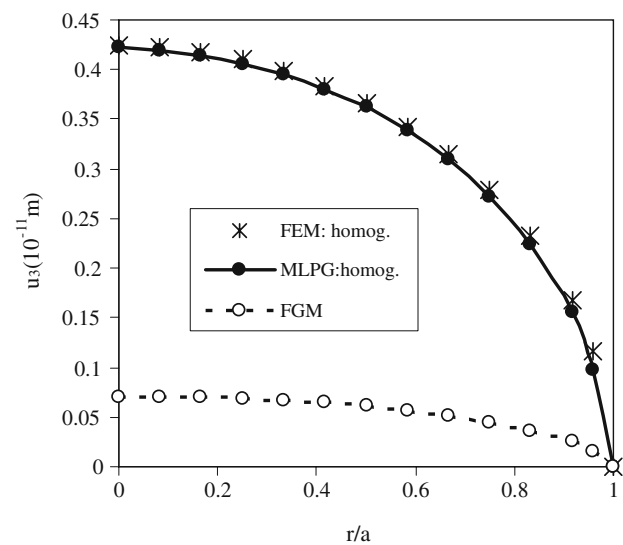


Fig. 16 Variation of the crack opening displacement with the normalized coordinate $r/2a$ in the cracked cylinder under a pure mechanical loading $\sigma_0 = 1$ Pa

homogeneous one. The maximum value of the SIF is only slightly reduced for the FGM cracked strip.

4.3 A penny-shaped crack in a finite cylinder

A penny-shaped crack in a finite cylinder as depicted in Fig. 15 is analyzed as the third example. The following geometry is considered: crack radius $a = 0.5$, cylinder radius $w = 1.25$, and cylinder length $2L = 3.0$. On the top of the cylinder either a uniform tension σ_0 , or a uniform magnetic induction B_0 are applied, firstly as static loads.

Also in this example, an exponential variation of the magneto-electro-elastic material parameters in radial direction is assumed, i.e.,

$$f_{ij}(r) = f_{ij0} \exp(\gamma r).$$

The material coefficients at the axis of symmetry corresponding to the $\text{BaTiO}_3\text{--CoFe}_2\text{O}_4$ composite are given by Wang and Mai [46]

$$\begin{aligned} c_{11} &= 22.6 \times 10^{10} \text{ Nm}^{-2}, & c_{13} &= 12.4 \times 10^{10} \text{ Nm}^{-2}, \\ c_{33} &= 21.6 \times 10^{10} \text{ Nm}^{-2}, & c_{44} &= 4.4 \times 10^{10} \text{ Nm}^{-2}, \\ c_{12} &= 12.5 \times 10^{10} \text{ Nm}^{-2}, & e_{15} &= 5.8 \text{ Cm}^{-2}, \\ e_{31} &= -2.2 \text{ Cm}^{-2}, & e_{33} &= 9.3 \text{ Cm}^{-2}, \\ h_{11} &= 5.64 \times 10^{-9} \text{ C}^2/\text{Nm}^2, & h_{33} &= 6.35 \times 10^{-9} \text{ C}^2/\text{Nm}^2, \\ d_{15} &= 275.0 \text{ N/Am}, & d_{31} &= 290.2 \text{ N/Am}, \\ d_{33} &= 350.0 \text{ N/Am}, \\ \alpha_{11} &= 5.367 \times 10^{-12} \text{ Ns/VC}, & \alpha_{33} &= 2737.5 \times 10^{-12} \text{ Ns/VC}, \end{aligned}$$

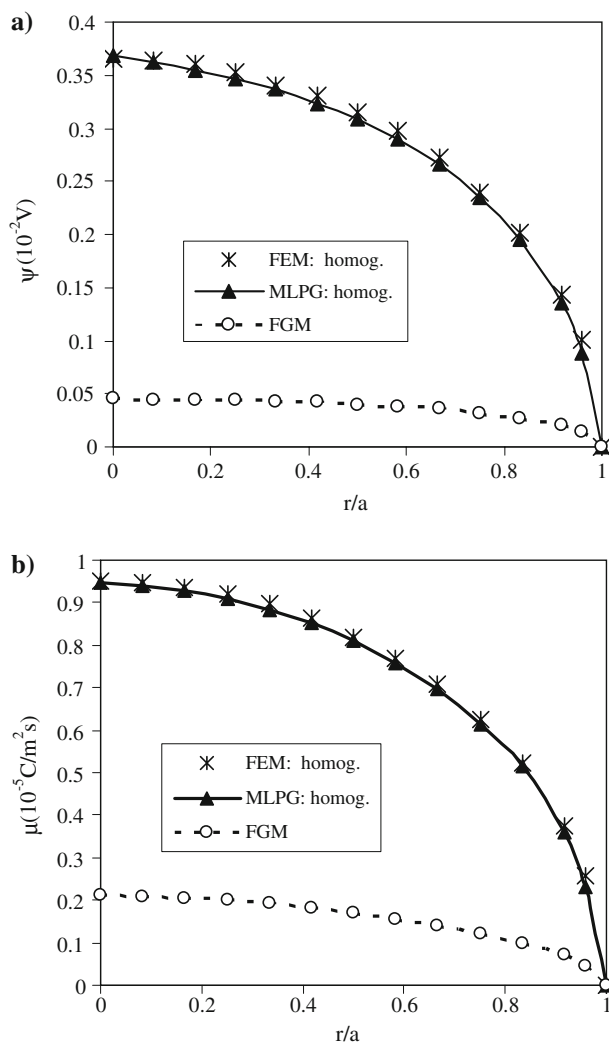


Fig. 17 Variation of **a** the electric, and **b** magnetic potentials with the normalized coordinate $r/2a$ under a pure mechanical loading $\sigma_0 = 1$ Pa in the cracked cylinder

$$\gamma_{11} = 81.0 \times 10^{-6} \text{Ns}^2\text{C}^{-2}, \quad \gamma_{33} = 83.5 \times 10^{-6} \text{Ns}^2\text{C}^{-2}, \\ \rho = 5500 \text{ kg/m}^3.$$

Numerical calculations are carried out for the gradient parameter $\gamma = 2$. A regular node distribution with 930 (31×30) nodes is used for the MLS-approximation of the displacements and the potentials in the analyzed domain ABCDE (see Fig. 15).

The static values of the SIF for the homogeneous and FGM cracked cylinder are $K_I^{\text{stat}} = 0.813 \text{ Pa m}^{1/2}$ and $K_I^{\text{FGM}} = 0.353 \text{ Pa m}^{1/2}$, respectively. The SIF in the cracked cylinder with positive material properties gradient is significantly reduced in comparison with the SIF for the corresponding homogeneous cylinder. This is due to the significant reduction of the crack opening displacement in the FGM cylinder as presented in Fig. 16. One can also see a good agreement

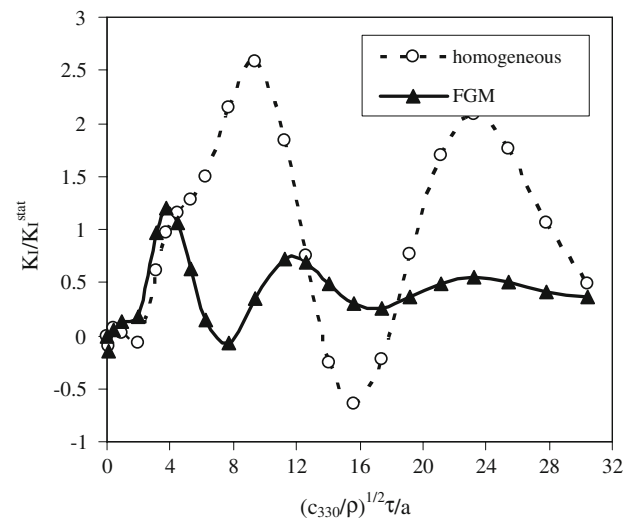


Fig. 18 Normalized stress intensity factor for a penny-shaped crack in a cylinder under a pure mechanical load $\sigma_0 H(\tau - 0)$

of numerical results obtained by the MLPG method and the FEM for a cracked homogeneous cylinder.

Variation of the electric and magnetic potentials with the radial coordinate under a pure mechanical loading $\sigma_0 = 1$ Pa is presented in Fig. 17. The EDIF and MIIF vanish in the static case with a pure mechanical load in the homogeneous cylinder. Both the electrical and magnetic potentials are significantly reduced in the FGM cylinder with respect to the homogeneous one. A good agreement between the MLPG and FEM results is again observed for both potentials in a homogeneous cylinder.

Next, the cracked cylinder is subjected to an impact mechanical load with Heaviside time variation and the intensity $\sigma_0 = 1$ Pa. Impermeable boundary conditions for the electric displacement and magnetic flux on crack surfaces are considered. The time variation of the normalized stress intensity factor is given in Fig. 18, where $K_I^{\text{stat}} = 0.813 \text{ Pa} \times \text{m}^{1/2}$ corresponds to the corresponding homogeneous case.

The peaks of the SIF in Fig. 18 for the FGM cylinder are significantly reduced with respect to the homogeneous case. The reduction is proportional to the reduction of the static SIF in both cases. If the dynamic SIF in the FGM cylinder is normalized by the corresponding static value $K_I^{\text{FGM}} = 0.353 \text{ Pa} \times \text{m}^{1/2}$ one obtains almost the same peak value as in the homogeneous case. The peak value of the SIF in FGM cylinder is reached at a shorter time instant than in the corresponding homogeneous one. It is due to the higher value of the wave velocity in the FGM cylinder than in the homogeneous one.

For the normalized EDIF and MIIF we have used parameters $\Lambda_e = e_{33}/h_{33}$ and $\Lambda_m = d_{33}/\gamma_{33}$, respectively. Numerical results are presented in Fig. 19. Opposite to the static case, finite values of EDIF and MIIF are obtained under a pure

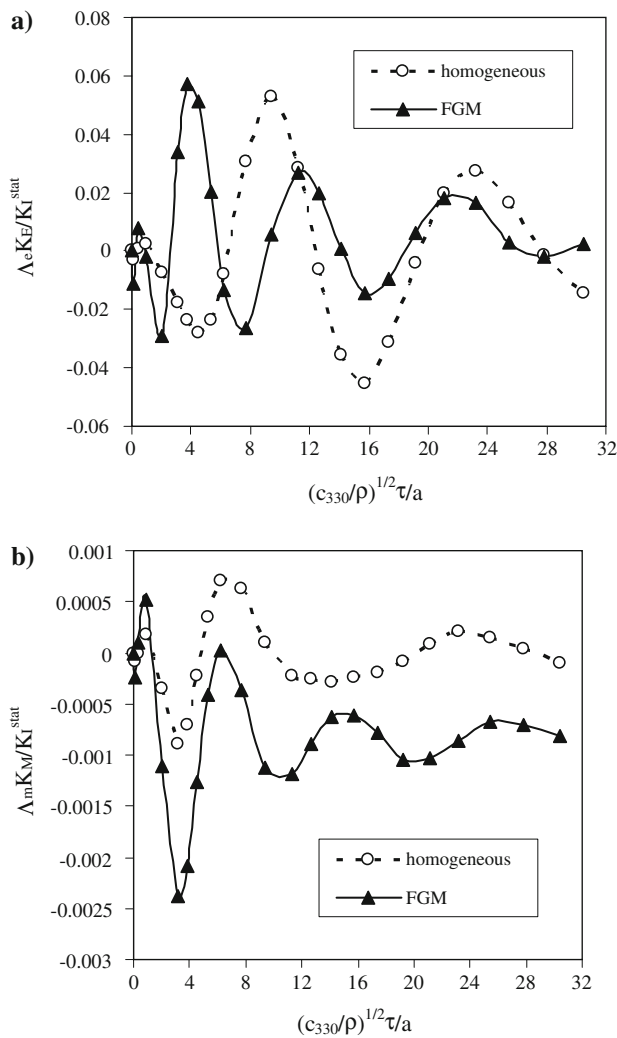


Fig. 19 Normalized **a** electric, and **b** magnetic intensity factors for a penny-shaped crack in a cylinder under a pure mechanical load σ_0 $H(\tau - 0)$

mechanical impact load in the homogeneous cylinder too. Both dynamic quantities for FGM cylinder are oscillating around the static values which are: $\Lambda_e K_E / K_I^{stat} = 0.00655$ and $\Lambda_m K_M / K_I^{stat} = -0.831 \times 10^{-3}$.

5 Conclusions

A meshless local Petrov–Galerkin method is presented for 2-D and 3-D axisymmetric crack problems in continuously nonhomogeneous and linear magneto-electric-elastic solids. Both static and transient dynamic loadings are considered. The analyzed domain is divided into small overlapping circular subdomains. A unit step function is used as the test function in the local weak-form of the governing partial differential equations. The derived local boundary-domain integral equations are nonsingular. The MLS scheme is

adopted for the approximation of the physical field quantities.

The present method provides an alternative numerical tool to many existing computational methods like the FEM or BEM. The main advantage of the present method is its simplicity. Compared to the conventional BEM, the present method requires no fundamental solutions and all integrands in the present formulation are regular. Thus, no special numerical techniques are required to evaluate the integrals. It should be noted here that the fundamental solutions are not available for magneto-electric-elastic solids with continuously varying material properties in general cases. The present formulation also possesses the generality of the FEM. Therefore, the method is promising for numerical analysis of multi-field problems like piezoelectric, electro-magnetic or thermoelastic problems, which cannot be solved efficiently by the conventional BEM.

An essential drawback of the present method is its larger computing time in comparison with the conventional domain-type discretization methods such as the FEM. The main reason is the fact that a meshless approximation usually involves more nodes and the required shape functions are more complex. To reduce the computing time, a mixed formulation can be applied, which reduces the radius of the support domain at the same accuracy as in the traditional approximation. Since a small size of the support domain decreases the bandwidth of the system matrix, the computing time can be significantly reduced. Therefore, future research efforts will be devoted to developing efficient meshless approaches in order to reduce its computing time.

Acknowledgments The authors acknowledge the support by the Slovak Science and Technology Assistance Agency registered under number APVV-20-035404, the Slovak Grant Agency VEGA-2/6109/6.

References

1. Alshits VI, Darinski AN, Lothe J (1992) On the existence of surface waves in half-anisotropic elastic media with piezoelectric and piezomagnetic properties. *Wave Motion* 16:265–283
2. Atluri SN (2004) The meshless method, (MLPG) for domain and BIE discretizations. Tech Science Press, Forsyth
3. Atluri SN, Han ZD, Shen S (2003) Meshless local Petrov–Galerkin (MLPG) approaches for solving the weakly-singular traction and displacement boundary integral equations. *CMES: Comput Model Eng Sci* 4:507–516
4. Atluri SN, Liu HT, Han ZD (2006) Meshless local Petrov–Galerkin (MLPG) mixed finite difference method for solid mechanics. *CMES: Comput Model Eng Sci* 15:1–16
5. Avellaneda M, Harshe G (1994) Magnetolectric effect in piezoelectric/magnetostriuctive multilayer (2–2) composites. *J Int Mater Syst Struct* 5:501–513
6. Belytschko T, Krogauz Y, Organ D, Fleming M, Krysl P (1996) Meshless methods; an overview and recent developments. *Comp Meth Appl Mech Eng* 139:3–47

7. Berlingcourt DA, Curran DR, Jaffe H (1964) Piezoelectric and piezomagnetic materials and their function in transducers. *Phys Acoust* 1:169–270
8. Chen JS, Wu CT, Yoon S, You Y (2001) A stabilized conforming nodal integration for Galerkin meshfree-methods. *Int J Numer Methods Eng* 50:435–466
9. Chung MY, Ting TCT (1995) The Green function for a piezoelectric piezomagnetic anisotropic elastic medium with an elliptic hole or rigid inclusion. *Philos Mag Lett* 72:405–410
10. Dolbow JE, Gosz M (2002) On computation of mixed-mode stress intensity factors in functionally graded materials. *Int J Solids Struct* 39:7065–7078
11. Du JK, Shen YP, Ye DY, Yue FR (2004) Scattering of anti-plane shear waves by a partially debonded magneto-electro-elastic circular inhomogeneity. *Int J Eng Sci* 42:887–913
12. Eringen CE, Maugin MA (1990) *Electrodynamics of Continua*. Springer, Berlin
13. Feng WJ, Su RKL (2006) Dynamic internal crack problem of a functionally graded magneto-electro-elastic strip. *Int J Solids Struct* 43:5196–5216
14. Feng WJ, Pan E, Wang X (2007) Dynamic fracture analysis of a penny-shaped crack in a magneto-electroelastic layer. *Int J Solids Struct* 44:7944–7955
15. Fleming M, Chu YA, Moran B, Belytschko T (1997) Enriched element-free Galerkin methods for crack tip fields. *Int J Numer Methods Eng* 40:1483–1504
16. Gao CF, Kessler H, Balke H (2003) Crack problems in magneto-electroelastic solids. Part I: Exact solution of a crack. *Int J Eng Sci* 41:969–981
17. Garcia-Sanchez F, Rojas-Diaz R, Saez A, Zhang Ch (2007) Fracture of magneto-electroelastic composite materials using boundary element method (BEM). *Theor Appl Fract Mech* 47:192–204
18. Garcia-Sanchez F, Saez A, Dominguez J (2005) Anisotropic and piezoelectric materials fracture analysis by BEM. *Comput Struct* 83:804–820
19. Han F, Pan E, Roy AK, Yue ZQ (2006) Responses of piezoelectric, transversely isotropic, functionally graded and multilayered half spaces to uniform circular surface loading. *CMES: Comput Model Eng Sci* 14:15–30
20. Hu KQ, Li GQ, Zhong Z (2006) Fracture of a rectangular piezo-electromagnetic body. *Mech Res Comm* 33:482–492
21. Landau LD, Lifshitz EM (1984) In: Lifshitz EM, Pitaevskii LP (eds) *Electrodynamics of continuous media*, 2nd edn. Pergamon Press, New York
22. Li S, Liu WK (2004) *Meshfree particle methods*. Springer, Berlin
23. Li JY (2000) Magneto-electroelastic multi-inclusion and inhomogeneity problems and their applications in composite materials. *Int J Eng Sci* 38:1993–2011
24. Liu JX, Liu XL, Zhao YB (2001) Green's functions for anisotropic magneto-electro-elastic solids with an elliptical cavity or a crack. *Int J Eng Sci* 39:1405–1418
25. Liu GR, Dai KY, Lim KM, Gu YT (2002) A point interpolation mesh free method for static and frequency analysis of two-dimensional piezoelectric structures. *Comput Mech* 29:510–519
26. Nan CW (1994) Magneto-electric effect in composites of piezoelectric and piezomagnetic phases. *Phys Rev B* 50:6082–6088
27. Niraula OP, Wang BL (2006) A magneto-electro-elastic material with a penny-shaped crack subjected to temperature loading. *Acta Mech* 187:151–168
28. Ohs RR, Aluru NR (2001) Meshless analysis of piezoelectric devices. *Comput Mech* 27:23–36
29. Pan E (2001) Exact solution for simply supported and multilayered magneto-electro-elastic plates. *ASME J Appl Mech* 68:608–618
30. Parton VZ, Kudryavtsev BA (1988) *Electromagnetoelasticity, piezoelectrics and electrically conductive solids*. Gordon and Breach Science Publishers, New York
31. Paulino GH, Jin ZH, Dodds RH (2003) Failure of functionally graded materials. In: Karihaloo B, Knauss WG (eds) *Comprehensive structural integrity*, vol 2. Elsevier, Amsterdam, pp 607–644
32. Sladek J, Sladek V, Atluri SN (2004) Meshless local Petrov–Galerkin method in anisotropic elasticity. *CMES: Comput Model Eng Sci* 6:477–489
33. Sladek J, Sladek V, Zhang Ch, Garcia-Sanchez F, Wünsche M (2006) Meshless local Petrov–Galerkin method for plane piezoelectricity. *CMC: Comput Mater Continua* 4:109–118
34. Sladek J, Sladek V, Zhang Ch, Sulek P, Pan E (2007) Evaluation of fracture parameters in continuously nonhomogeneous piezoelectric solids. *Int J Fract* 145:313–326
35. Sladek J, Sladek V, Hellmich Ch, Eberhardsteiner J (2007) Heat conduction analysis of 3D axisymmetric and anisotropic FGM bodies by meshless local Petrov–Galerkin method. *Comput Mech* 39:323–333
36. Song ZF, Sih GC (2003) Crack initiation behavior in magneto-electroelastic composite under in-plane deformation. *Theor Appl Fract Mech* 39:189–207
37. Stehfest H (1970) Algorithm 368: numerical inversion of Laplace transform. *Comm Assoc Comput Mach* 13:47–49
38. Su RKL, Feng WJ (2007) Transient response of interface cracks between dissimilar magneto-electro-elastic strips under out-of-plane mechanical and in-plane magneto-electrical impact loads. *Comput Struct* 78:119–128
39. Suresh S, Mortensen A (1998) *Fundamentals of functionally graded materials*. Institute of Materials, London
40. Tian WY, Gabbert U (2005) Macro-crack-micro-crack problem interaction problem in magneto-electroelastic solids. *Mech Mater* 37:565–592
41. Tian WY, Rajapakse RKND (2005) Fracture analysis of magneto-electroelastic solids by using path independent integrals. *Int J Fract* 131:311–335
42. Ueda S (2003) Crack in functionally graded piezoelectric strip bonded to elastic surface layers under electromechanical loading. *Theor Appl Fract Mech* 40:225–236
43. Wang X, Shen YP (2002) The general solution of three-dimensional problems in magneto-electroelastic media. *Int J Eng Sci* 40:1069–1080
44. Wang BL, Mai YW (2003) Crack tip field in piezoelectric/piezomagnetic media. *Eur J Mech A/Solids* 22:591–602
45. Wang BL, Han JC, Mai YW (2006) Mode III fracture of a magneto-electroelastic layer: exact solution and discussion of the crack face electromagnetic boundary conditions. *Int J Fract* 139:27–38
46. Wang BL, Mai YW (2007) Applicability of the crack-face electromagnetic boundary conditions for fracture of magneto-electroelastic materials. *Int J Solids Struct* 44:387–398
47. Zhao MH, Yang F, Liu T (2006) Analysis of a penny-shaped crack in a magneto-electro-elastic medium. *Philos Mag* 86:4397–4416
48. Zhou ZG, Wang B, Sun YG (2004) Two collinear interface cracks in magneto-electro-elastic composites. *Int J Eng Sci* 42:1155–1167
49. Zhu B, Qin T (2007) Application of hypersingular integral equation method to three-dimensional crack in electromagnetothermoelastic multiphase composites. *Int J Solids Struct* 44:5994–6012
50. Zhu X, Wang Z, Meng A (1995) A functionally gradient piezoelectric actuator prepared by metallurgical process in PMN-PZ-PT system. *J Mater Sci Lett* 14:516–518